

Contents — P

The Global Three Dimensional Distribution and Temperature of Near-Surface Martian Ground Ice: New Results from MGS TES <i>D. A. Paige and J. M. Scherbenski</i>	3265
MarsFlo: A General Tool for Simulating Hydrological Processes in the Subsurface of Mars <i>S. L. Painter</i>	3161
From the South Pole to the Northern Plains: The Argyre Planitia Story <i>T. J. Parker, J. A. Grant, F. S. Anderson, and W. B. Banerdt</i>	3274
Stratigraphic Implications of the Relaxation of Troughs and Scarps Within the Martian North Polar Layered Deposits <i>A. V. Pathare and D. A. Paige</i>	3084
Testing the Pseudocrater Hypothesis <i>M. C. Payne and J. D. Farmer</i>	3070
Viscous Flow of Ice-rich Crater Fill Deposits and Periodic Formation of Protalus Ramparts: A Climate Record? <i>J. T. Perron, A. D. Howard, and W. E. Dietrich</i>	3236
Noachian Evolution of Mars <i>R. J. Phillips, C. L. Johnson, B. M. Hynek, and B. M. Jakosky</i>	3021
Polygonal Landforms at the South Pole and Implications for Exposed Water Ice <i>S. Piqueux, S. Byrne, and M. I. Richardson</i>	3275
Automated Feature Extraction and Hydrocode Modeling of Impact Related Structures on Mars: Preliminary Report <i>C. S. Plesko, E. Asphaug, S. P. Brumby, and G. R. Gisler</i>	3227
The Composition of Martian Low Albedo Regions Revisited <i>F. Poulet and S. Erard</i>	3110
Mid-Latitude Composition of Mars from Thermal and Epithermal Neutrons <i>T. H. Prettyman, W. C. Feldman, R. C. Elphic, W. V. Boynton, D. L. Bish, D. T. Vaniman, H. O. Funsten, D. J. Lawrence, S. Maurice, G. W. McKinney, K. R. Moore, and R. L. Tokar</i>	3253
Thermophysical Properties of the Martian South Polar Region <i>N. E. Putzig, M. T. Mellon, and R. E. Arvidson</i>	3173

THE GLOBAL THREE DIMENSIONAL DISTRIBUTION AND TEMPERATURE OF NEAR-SURFACE MARTIAN GROUND ICE: NEW RESULTS FROM MGS TES. D. A. Paige and J. M. Scherbenski¹

¹Dept. of Earth and Space Sciences, UCLA, Los Angeles, CA 90095. dap@mars.ucla.edu

Summary: We have discovered significant global-scale seasonal thermal anomalies in the MGS TES surface temperature observations that coincide spatially with the Odyssey GRS observations of enhanced near-surface hydrogen abundance [1]. The TES thermal anomalies can be explained quantitatively by the widespread presence of cold, high thermal inertia material within millimeters to centimeters of the surface that we interpret as evidence for ground ice that must extend to depths of many meters. The results provide significant insights into the properties and processes that govern the behavior of Martian water under current climatic conditions, the surface geology of the planet, as well as much higher resolution Martian ground ice maps than have been previously available.

Details: Using techniques originally developed for the analysis of Viking IRTM data [1] [2], TES diurnal and seasonal temperature variations are compared to the results of a one-dimensional radiative-convective model, and best-fit surface thermal and reflective properties are mapped. The baseline thermal model includes the radiative and convective effects of the Martian atmosphere, and assumes surface thermal properties that are homogenous with depth. Seasonal thermal anomalies are identified by comparing the best-fit baseline model-derived albedos with the measured TES albedos. Such a comparison reveals the presence of significant (5-10K) thermal anomalies at a wide range of latitudes. Both negative and positive anomalies are observed, depending on latitude and season, and these anomalies are well correlated with the hydrogen abundance maps produced by GRS.

To map the depth to the ground ice, the TES data are compared to the results of a more sophisticated model with surface thermal properties that are inhomogeneous with depth. In this two-layer model, a low thermal inertia surface layer is assumed to overlie high thermal inertia material that extends to great depth below. The depth to the high inertia material is a free parameter, which can be determined for each mapped region by first constraining the inhomogeneous model's surface albedo to equal the TES measured albedo, and then comparing the model's predicted diurnal and seasonal surface temperatures to those observed by TES. In regions where thermal anomalies are observed, the two-layer model provides much better fits to the TES observations than the homogeneous model.

The results of the fitting procedure yield three distinct types of data products – all of which can be produced as a function of Martian season. The first are maps of the thermal inertia of the surface layer. The second are maps of the depth to the high thermal inertia subsurface layer. The third are maps of the temperature of the top of the high thermal inertia subsurface layer. In the model, the thermal inertia of the subsurface layer is not directly constrained by observations. However, the magnitude lower layer's effect on surface temperatures is proportional to the lower layer's thermal inertia, so at any location, a minimum value can be found. Furthermore, the maximum possible thermal inertia for the lower layer is bounded by the maximum possible thermal inertia of rock/ice. If the high thermal inertia subsurface material is assumed to contain water ice, maps of model-predicted annual maximum temperatures for the top lower layer can be used to estimate implied near-surface water frost-point temperatures. This provides constraints on the abundance of near-surface water vapor in the atmosphere assuming that the ice is close to being in equilibrium with the present climate.

Implications: Our analysis of the TES observations provides additional strong evidence for the widespread global-scale presence of near-surface ground ice on Mars. The ice has high thermal inertia, which is consistent with GRS results indicating high water to soil ratios [1]. The maps we will present at the meeting will show significantly more spatially resolved, three-dimensional views of the present distribution of Martian ground ice than have been available previously. These maps will be correlated with topography, images, geological maps, soil thermal and reflectance properties, and atmospheric water vapor abundance datasets, to produce a much clearer picture of the properties and processes that are responsible for its global distribution.

References: [1] Boynton et al., *Science* 297, 81-85, 2002. [2] Paige, D. A., J. E. Bachman and K. D. Keegan, *J. Geophys. Res.* 99, 24,959-25,991, 1994. [3] Paige, D. A. and K. D. Keegan, *J. Geophys. Res.* 99, 24,993-26,013, 1994.

MARSFLO: A GENERAL TOOL FOR SIMULATING HYDROLOGICAL PROCESSES IN THE SUBSURFACE OF MARS. S. L. Painter, Southwest Research Institute (6220 Culebra Road, San Antonio, Texas 78238-5166 spainter@swri.org).

Introduction: Although recent spacecraft observations have provided important new information about the present state of the near-surface hydrological system [1], significant uncertainties about the deeper hydrological system and the past system remain. Numerical simulations used in combination with spacecraft or lander-based observations have an important role in testing hypotheses and in placing constraints on the hydrological system. Previous modeling studies have relied on computer codes designed to address specific processes, usually in one spatial dimension (e.g. [2,3]) but occasionally in three dimensions [4]. General-purpose simulation codes addressing the range of relevant physical processes and conditions in the Martian subsurface conditions have yet to be developed.

The Southwest Research Institute™ is currently developing a non-isothermal, multiphase simulation code adapted for the conditions of the Martian subsurface. The goal is to provide the Mars research community with a general simulation tool (MarsFlo) that can be used to test hypotheses about the current and past state of the Mars subsurface hydrological environment in multiple spatial dimensions.

Underlying Models in the MarsFlo Code: The processes included in the MarsFlo code include:

- Partitioning of water between the liquid, vapor, and ice phases, including the effect of capillary forces on lowering the vapor pressure.
- Advective transport in the liquid and gas phases.
- Diffusive transport of water vapor and CO₂ in the gas phase and of CO₂ dissolved in liquid water.
- Conductive and convective transport of heat.
- Accurate representations of various physical properties of water/ice/vapor as functions of temperature and pressure.

Conservation Equations. The governing equations for MarsFlo include an energy balance equation, and conservation equations for water and CO₂ in gas, liquid, and ice phases. In partially saturated pores, water and/or ice is assumed to be in equilibrium with water vapor, which is why only two conservation equations are required.

Using the extended Darcy's law for multiphase flow, the conservation equations for water and CO₂ are:

$$\frac{\partial}{\partial t} \left[\sum_{p=l,g,i} \phi \omega_p^j \rho_p s_p \right] = \sum_{p=l,g} \left(\nabla \cdot \left[\frac{\omega_p^j \rho_p k_{rp} k}{\mu_p} \nabla (P_p + \rho_p g z) \right] \right) + \sum_{p=l,g} \nabla \cdot \left[\phi \rho_p s_p \tau_p D_p^j \nabla \omega_p^j \right] + S^j \quad \text{for } j = w, a \quad (1)$$

where s is the phase saturation, t is time, ϕ is porosity, ρ is the phase density, ω is mass fraction, k is the absolute permeability, k_r is relative permeability, μ is dynamic viscosity, z is the vertical coordinate, g is the acceleration due to gravity, D is the diffusion coefficient, τ is the tortuosity factor, and S is the mass source rate. The subscripts l , g , and i represent liquid, gas and ice phases, respectively. The superscripts w and a represent water and CO₂ mass, respectively.

The corresponding energy balance equation is

$$\frac{\partial}{\partial t} \left[\sum_{p=l,g,i} (\phi \rho_p s_p u_p) + (1 - \phi) \rho_s u_s \right] = - \sum_{p=l,g} \nabla \cdot (\rho_p h_p \mathbf{V}_p) + \nabla \cdot [k_e \nabla T] + S_E \quad (2)$$

where u is internal energy, h is enthalpy, \mathbf{V} is the darcy flow velocity, k_e is the equivalent thermal conductivity for the rock-water-ice mixture, S_E is the thermal energy source, and the subscript s denotes the solid (rock) phase.

Several constitutive relations are needed to close the above system. The most important of these are the saturation-pressure relations and the relative permeability-saturation relations. The models implemented in MarsFlo follow closely those of White [5], which were synthesized from existing theories on freezing in terrestrial soils [6,7].

Saturation Pressure Relationships. Functional relations between phase saturations and interphase capillary pressures are required. In partially frozen geological material, water is generally the wetting phase with respect to both air and ice, implying that ice forms first in the largest water-filled pores. It is also generally assumed that a thin film of water separates the ice from gas and prevents a direct gas-ice interface. Thus, two

retention curves (saturation-capillary pressure relations) are required.

In multiphase systems, the retention curves for all phase pairs can be related to the retention curve for any two-phase system by an interfacial-tension dependent rescaling of the capillary pressure. For the ice-water-gas system,

$$\frac{s_l}{s_l + s_i} = S_*(\beta P_{cil}) \quad (3)$$

$$\frac{s_l}{1 - s_i} = S_*(P_{cgl}) \quad (4)$$

where S_* is the retention curve for a two-phase system with unfrozen liquid and gas, β is the ratio of interfa-

cial tensions $\frac{\sigma_{gl}}{\sigma_{il}}$, P_{cgl} is the gas-liquid capillary pres-

sure and P_{cil} is the ice-liquid capillary pressure. The left side of equation 3 is the ‘‘unfrozen fraction’’ and the left side of equation 4 is the ‘‘apparent’’ liquid saturation (ratio of unfrozen liquid to available pore space). For clarity, we have set the residual (irreducible) saturation to zero, but this can easily be included as discussed by White [5].

The ice-liquid capillary pressure can be obtained from thermodynamic considerations, as derived by Loch [8]

$$P_i = \rho_i \left[\frac{P_i - C_i RT}{\rho_l} - h_{iw}^0 \ln \left(\frac{T}{T^0} \right) \right] \quad (5)$$

where C_i is the solute concentration, R is the universal gas constant, h_{iw} is the heat of fusion for water-ice, and the superscript 0 represents reference conditions. In this preliminary study, we set the solute concentration to zero. However, solute exclusion from the ice phase and the resulting increase in the aqueous concentration has the important effect of lowering the freezing temperature and will be included in future refinements of the model.

Several empirical forms exist for the soil moisture retention curve S_* . Van Genuchten’s [9] model is used,

$$S_*(P_c) = \left[1 + (\alpha P_c)^n \right]^{-m} \quad \text{for } P_c > 0 \quad (6)$$

$$S_*(P_c) = 1 \quad \text{for } P_c \leq 0$$

where α and n are curve fitting parameters and $m = 1 - 1/n$.

Examples showing the unfrozen fraction as function of temperature are shown in Figure 1 for various values of the van Genuchten parameters. These were obtained by combining equations 3,5 and 6.

Relative Permeability Curves. Relationships between the phase permeabilities and the phase satura-

tions are also required. Once the saturation-capillary pressure relationships have been specified, Mualem’s model [10] can be used to calculate the liquid relative permeability. The result is

$$k_{rl} = (s_l)^{1/2} \left[1 - \left(1 - (s_l)^{1/m} \right)^m \right]^2 \quad (7)$$

Gas-phase relative permeability is generally less important and we use a simple linear relationship $k_{rg} = s_g$.

Gas Diffusion Model. In the low pressures of Mars, the mean free path for gas molecules is roughly the same magnitude as a typical pore size [2]. Under these conditions, gas diffusion results from a combination of classical binary molecular diffusion and collisions with the mineral grains (Knudsen diffusion). The diffusion coefficient is calculated in Marsflo as an appropriately weighted combination of binary molecular diffusion and Knudsen diffusion [2].

Thermal Conductivity Model. Thermal conductivity in porous media depends on the properties of the mineral grains, the pore structure, and properties of the pore-filling fluids. Because MarsFlo is designed to operate across the entire range of phase saturations – from fully saturated with ice and/or water to fully dry – thermal conductivity models that can be tuned continuously across these saturation states are required. The thermal conductivity model in MarsFlo is based on a series-parallel model that is generalized slightly from that of Mellon et al. [3]. The model considers the bulk (composite) thermal conductivity of a porous medium as being due to two thermal resistances in series, one for the mineral grains and one for the interstitial resistance to heat flow. The interstitial resistance is composed in turn of three resistors in parallel: a gap resistance, ice resistance and water resistance. Each of these individual resistors depends on the local porosity and the phase saturations. Specifically, the composite conductivity is written

$$\kappa = \frac{\kappa_{\text{int}} \kappa_{\text{grain}}}{\phi \kappa_{\text{grain}} + (1 - \phi) \kappa_{\text{int}}} \quad (8)$$

where κ_{grain} is the thermal conductivity for the mineral grains, ϕ is the porosity, and κ_{int} is the interstitial conductivity. Under totally dry conditions, κ_{int} is simply a gap conductance κ_{gap} but in partially saturated conditions it depends on the local phase saturations and the thermal conductivities for liquid and ice:

$$\kappa_{\text{int}} = (1 - f_i - f_l) \kappa_{\text{gap}} + f_l \kappa_l + f_i \kappa_i \quad (9)$$

where f_i and f_l are fraction of the cross sectional area available for liquid conductance through the ice and liquid phases, respectively. Mellon et al. [3] note that

the cross sectional area fraction occupied by the wetting phase is well approximated by the square root of the saturation for that phase. For the ice-water-gas system with wetting hierarchy water>ice>gas, this implies $f_l \cong \sqrt{s_l}$ and $f_i \cong \sqrt{s_i + s_l} - \sqrt{s_l}$.

Thermophysical Properties. Accurate representations of various thermophysical properties such as saturated vapor pressure, density, internal energy, specific heat are also needed. These are included in MarsFlo through empirical fits to tabulated values.

Numerical and Computational Considerations.

The integrated finite difference method is used in MarsFlo to discretize the conservation equations. In this approach, the partial differential equations are replaced by a coupled set of discrete balance equations, one for each component in each cell. This spatial discretization approach is more difficult to implement than a finite difference method on a simple structured grid, but has the advantage of accepting structured or fully unstructured grids in one, two or three dimensions.

Time stepping in MarsFlo is by the fully implicit method with Newton iterations at each time step to resolve the nonlinearities, consistent with the approach normally used in two-phase thermal hydrological systems. Calculation of the Jacobian matrix used in the Newton method is done numerically by the perturbation method.

Primary variables in MarsFlo depend on the saturation state, and a variable switching method is used to accommodate changes in the saturation state. In the all-gas conditions, the primary variables are air partial pressure, total gas pressure, and temperature. For partially saturated conditions, the primary variables are gas saturation, gas pressure, and temperature. In the no-gas state, the primary variables are mole fraction of CO₂ in liquid, pressure, and temperature. Secondary variables are calculated at each time from these primary variables using the constitutive relationships.

Example Simulations: *Laboratory Freezing Experiment.* As an initial test of the MarsFlo code, we attempt to reproduce, in general terms, freezing phenomena observed in laboratory experiments, similar to those of Jame and Norum [11]. The particular scenario modeled involves a 30 cm long tube filled with a partially saturated porous medium. The ends of the tube are sealed and the medium is initially at 20 °C with liquid saturation of 0.27. At $t=0$, the temperature at one end is lowered to -10 °C. The temperature of the other end is held constant at 20 °C. Parameters for this simulation are the same as those of White [5]: $\alpha=0.279 \text{ m}^{-1}$, $n=1.64$, $\phi=0.50$, $k=3.0 \cdot 10^{-10} \text{ m}^2$.

Results are shown in Figure 2 for times 6 hours and 24 hours. The simulation reproduces moisture redistribu-

tion phenomena that are observed experimentally. As the freezing front propagates into the medium, the liquid saturation is reduced by freezing. This greatly decreases the liquid pressure, and draws water into the freezing front, eventually increasing the total water content at the position of the freezing front and decreasing the water content ahead of the freezing front. This simulation is generally consistent with the experimental results of Jame and Norum [11]; direct quantitative comparisons were not attempted because of incomplete information about the experimental conditions.

Freezing of a Martian Aquifer. For a second demonstration example, we consider the freezing of an aquifer and the long-term redistribution of ice in the Martian subsurface.

The model domain is one-dimensional with a no-flow boundary for gas and liquid at the bottom, which is located at 1265 meters below the surface. The initial condition is steady state with water table located about 500 m below the surface. The initial surface temperature is 273.65 K and a geothermal flux of 30 mW/m² is applied at the lower boundary. The dry thermal conductivity is 1 W/m² K. Under these steady state conditions, the bottom of the simulation domain has temperature of about 298 K.

To start the simulation, the surface temperature is lowered to -30 °C. The upper boundary is also closed to vapor movement, an imposed condition that is meant to represent the formation of a vapor barrier such as an ice layer on the surface. The results are shown in Figure 3 for several selected times. For the first few hundred years, the cold front is propagating into the subsurface, essentially freezing the small quantities of water in place. At about 1000 years (not shown), the 0 °C isotherm starts to approach the water table. As ice starts to form a few meters above the water table, capillary forces draw water into the freezing zone. At about 2000 years, enough liquid water have been drawn from the saturated zone into the freezing zone to cause the pore space becomes saturated with ice at one location. This process of freezing and freezing-induced redistribution of water continues until the entire aquifer is frozen (about 10000 years). Once the entire aquifer is frozen, the thermally driven redistribution of water does not stop, but continues at a much slower rate. Under these conditions, thermally driven vapor diffusion causes ice to migrate from the ice layer at depth to the colder regions near the surface. Over 20 Million years, this cold trap effect moves enough water to nearly saturate the pore space with ice near the surface.

Conclusions: Prototype versions of the MarsFlo code demonstrate the feasibility of adapting the theory of terrestrial freezing soils to Martian conditions.

MarsFlo has a wide range of potential applications. It may be used, for example, to:

- test hypotheses about the evolution of the subsurface hydrological environment,
- refine estimates of the depth to unfrozen water,
- study interactions between hypothesized magmatic intrusions and the cryosphere,
- evaluate the potential for future drilling activities to make unwanted perturbations to the in-situ environment.

Future development of the MarsFlo code will focus on improving numerical performance, on models for atmosphere/subsurface interactions, and on coupling with geochemistry codes.

References:

- [1] Boynton W.V. et al. (2002) *Science*, 297, 81-85. [2] Clifford S. M. (1991) *GRL*, 18(11), 2055-2058. [3] Mellon, M. T. and Jakosy, B. M. (1993) *JGR*, 98(E2), 3345-3364. [4] Travis B. (2002) *EOS Trans. AGU*, 83(47) *Fall Meet. Suppl.*, Abstract P12A-0358. [5] White M. D. 1995 In *Proceedings of Fifteenth Annual American Geophysical Union Hydrology Days*. [6] Miller R.D. (1980) in *Applications in Soil Physics*, eds. D. Hillel. 254-299. Academic Press, New York. [7] Panday S. and Corapcioglu M. Y. (1994) *J. Contam. Hydrology*, 16, 235-269. [8] Loch J.P.G. (1997) *Soil Sci.*, 126, 77-80. [9] Van Genuchten, M. T. (1998) *Soil Sci. Soc. Am. J.*, 44, 892-898. [10] Mualem, Y. (1976) *Water Resour. Res.*, 12, 513-522. [11] Jame, Y.W. and Norum, D.I. (1980) *Water Resour. Res.* 9(5), 1314-1323.

Additional Information: The author is grateful to Cynthia Dinwiddie for developing fits for saturated vapor pressure. I also thank Gary Walter and Budhi Sagar for reviewing the manuscript and the Southwest Research Institute Initiative on Mars (SwIM) for supporting this work.

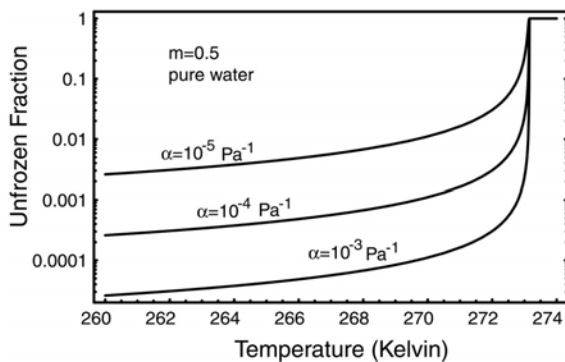


Figure 1: Unfrozen liquid fraction versus temperature for three values of the van Genuchten parameter.

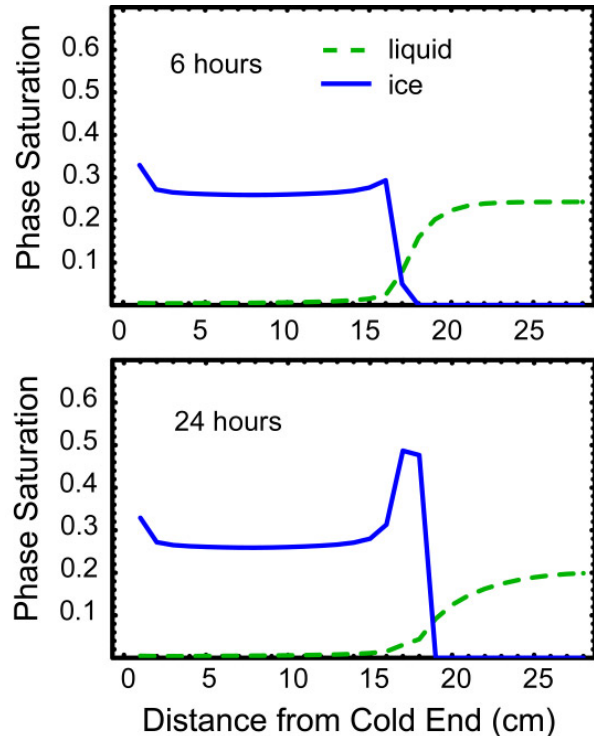


Figure 2: MarsFlo simulation of freezing porous medium at the laboratory scale showing experimentally observed phenomena of freezing-induced moisture redistribution.

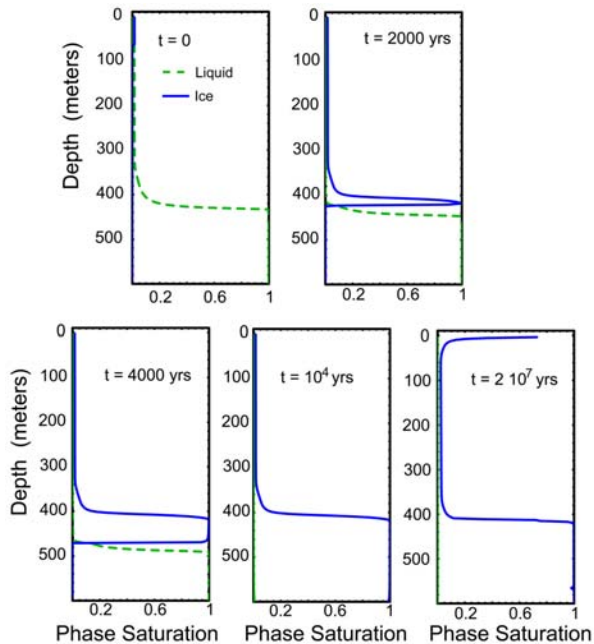


Figure 3: Simulation of a freezing aquifer and long-term redistribution of moisture in the Martian subsurface. This demonstration simulation spans the range of physical conditions (all gas, all liquid, all ice, partially saturated) expected in the Martian subsurface.

FROM THE SOUTH POLE TO THE NORTHERN PLAINS: THE ARGYRE PLANITIA STORY. T. J.

Parker¹, J. A. Grant², F. S. Anderson³ and W. B. Banerdt², ¹Jet Propulsion Laboratory, California Institute of Technology, 4800 Oak Grove Dr., Pasadena, CA 91109, timothy.j.parker@jpl.nasa.gov, ²Center for Earth and Planetary Studies, Smithsonian Inst., 4th and Independence SW, Washington, D.C. 20560-0315, ³University of Hawai'i at Manoa, Hawai'i Institute of Geophysics and Planetology, 1680 East-West Road, POST 526B, Honolulu, HI 96822.

Introduction: Parker (1985, 1994) first described evidence for catastrophic flooding from a large lake or sea within Argyre Planitia through the Uzboi-Holden-Ladon-Margaritifer Valles system during the Noachian. The channel connection to Argyre had been recognized during the mid-1970s, based primarily on Russian orbiter images taken at that time (Kuzmin, pers. comm.). The most critical reviews of these inferences related to the relative timing of the plains materials, sinuous ridges, and debris aprons in southern Argyre, and the connection, via Uzboi Vallis, of ponding within Argyre to flooding through the Chryse Trough. The prevailing "competing" hypothesis for formation of materials within Argyre is that they are a result of south circumpolar glacial processes, with glacial scour and stagnation producing the pitting and sinuous ridges (eskers) on the basin floor (e.g., Kargel and Strom 1992) rather than lacustrine erosion and deposition followed much later by a process akin to rock glacier formation of the debris aprons in a colder Amazonian climate. Argyre was part of a larger surface hydrological system (the Chryse Trough (Saunders, 1979) that also included two large valley networks draining the Margaritifer Sinus region northwest of Argyre. The morphometry of these systems suggest a combination of precipitation and groundwater sapping, with surface runoff for their formation (Grant and Parker 2002).

Real Topography! The inference that a sea within Argyre drained catastrophically through Uzboi Vallis could not be verified with the low-resolution topography available prior to MOLA, because the source of Uzboi is obscured by two large craters (Hale and Bond) where it approaches Argyre's north rim, and the downstream end is overlain by Holden Crater. Viking data doesn't clearly show which way Uzboi Vallis flowed.

Results from the MGS mission (and now the Mars Odyssey Mission) offered the opportunity to revisit the controversial origin and timing of putative sedimentary deposits within Argyre, and test the inferences made about the history of fluvial and lacustrine degradation of the basin and Chryse Trough that were made by Parker based on Viking data.

Argyre Basin and the Chryse Trough Channel Systems: Argyre lies at the southern end of the "Chryse Trough," a broad topographic trough identified based on the Mariner 9 and Viking low-resolution

topography (Fig. 6) which dips gently northward from Nereidum Montes to Chryse Planitia (Saunders 1979). The Mariner 9 and Viking Orbiter-based topographic maps that were available prior to MOLA were not of sufficient quality to map the continuity of this channel system, or even to verify that Uzboi Vallis flowed out of Argyre rather than into it. The new data from MOLA and MOC (and now THEMIS) is of sufficiently high resolution that this and a number of other nagging questions regarding Argyre Basin evolution and associated channels can now be addressed in detail. Geomorphic observations by Parker (1985, 1994), coupled with the global hydrologic models of Clifford and Parker (2001) and the MOLA topography appear to confirm that Argyre and the channels flowing into and out of it comprise the longest known fluvial system in the solar system.

Valley Networks draining into Argyre: Three large valley networks and two outflow channels cut through the rim of Argyre on its southeast and north sides. The three valley networks – Surlius Valles, Dzígai Valles, and Palacopas Valles – all drain into Argyre from the south and east, through the southern rim mountains (Charitum Montes). Parker (1997) suggested that these valleys once flowed outward from the rim of Argyre during the early Noachian, but that they were captured by steeper interior-draining systems that eroded headward into the rim mountains more quickly than the outward-draining systems advanced headward, also during the Noachian. Surlius and Dzígai Valles both head near the Dorsa Argentea Formation (Tanaka and Scott, 1987). This formation may be the remnants of a circumpolar lake or sea that overtopped the drainage divides at the heads of Surlius and Dzígai Valles.

Since this formation appears, for the most part, to be relatively flat-lying sediment occupying several broad intercrater depressions in the south polar region, we infer this lacustrine origin. Based on the hydrologic model described in Clifford and Parker (2001), we propose that large volumes of basal meltwater may have been discharged to the surface from beneath the south polar cap when the rate of basal melting exceeded the infiltration rate of the underlying crust (necessary, unless polar temperatures were above freezing at the time). Such conditions are a plausible consequence of the planet's higher early geothermal heat flux and the high rates of polar deposition that are

thought to have occurred at this time. The resulting lakes formed by this discharge would have spilled over local topographic divides into neighboring basins. But the topographic divide between the Dorsa Argentea Formation and Hellas Basin appears to be slightly higher (in the global topography) than that between the formation and Argyre Basin, and no channeling is evident into Hellas. Once Argyre captured drainage from the south polar region and was itself filled, catastrophic overflow through the Chryse Trough could commence.

Catastrophic flooding out of Argyre: The two outflow channels radial to Argyre are Nia Valles and Uzboi Vallis. Nia Valles is a relatively fresh-looking, small outflow channel that superposes the mouth of Palacopas Valles in southeast Argyre, south of Galle Crater. Nia Vallis probably formed during the early Amazonian, after the major fluvial and lacustrine episodes had concluded (Parker 1989, 1994), and is unrelated to flow out of the basin.

Uzboi Valles flowed into Holden Basin prior to formation of Holden Crater (Parker 1985). The northeast rim of Holden Basin is “gone” even though this basin superposes Ladon Basin. Instead, a broad “ramp” was identified in Viking Orbiter stereo pairs by Parker (1985). Ladon and Arda Valles converge on this ramp and drain into the interior of Ladon Basin. Parker (1985) inferred that the rim of Holden Basin failed catastrophically during flooding from Argyre to produce this ramp, which drained a temporary lake that had formed in Holden Basin. Continued flooding from Uzboi Vallis favored Ladon Valles’ course, so Arda Valles was quickly abandoned. Channel morphology disappears just inside the inner rim of Ladon Basin, but resumes on the basin’s northeast side, at Margaritifer Valles (Grant 1987).

The “Mouth” of Margaritifer Valles: Margaritifer Valles quickly branches into a large, complex distributary system at about 13°S, 24°W, that broadens to about 300 width and eventually fades into the highland terrain around 8°S, 23°W (MDIM-1 Areographic). Individual branches of Margaritifer Valles exhibit two distinct preservation states – one that appears sharply defined and another that is quite subdued with walls that often appear “gullied”. Uzboi and Ladon Valles similarly show two distinct morphologies, suggesting there were at least two catastrophic flood episodes from Argyre (Parker 1985).

The termination of Margaritifer Valles coincides with the location of the proposed “Meridiani Shoreline” (Clifford and Parker 2001), or Meridiani Level, the westward extension of a contact separating subdued highlands on the north from “rugged,” channeled highlands to the south in Terra Meridiani (Edgett and Parker 1997).

The implication of this distributary pattern to distal Margaritifer Valles is that it may represent a delta that formed where catastrophic flooding from Argyre reached its base level in an ocean occupying the northern plains to about the -1500m elevation. The Meridiani Level is the highest stand of the ocean proposed by Parker et al. (1989, 1993) that had been proposed prior to preparation of this proposal.

Ares Valles originates at 2°S 18°W, from Iani and Margaritifer Chaos, and flows north through the Chryse Trough, Through Chryse Planitia and disappears in Acidalia Planitia at 32°N, 29°W. Ares is a younger channel than Margaritifer Valles, however, as the Chaotic Terrains from which it flows formed at the expense of the terrain that is cut by Margaritifer Valles (i.e., the floor of Margaritifer Valles is consumed by collapse of the chaotic terrain). So Ares Valles post-dates the proposed Meridiani Level feature. It also post-dates the Arabia Level (above), and may be contemporaneous with the Deuteronilus Level (Clifford and Parker 2001).

References: Clifford, S. M., and T. J. Parker. The Evolution of the Martian Hydrosphere: Implications for the Fate of a Primordial Ocean and the Current State of the Northern Plains, in press, Icarus, 2001.

Edgett, K. S., and T. J. Parker. Water on early Mars: Possible subaqueous sedimentary deposits covering ancient cratered terrain in western Arabia and Sinus Meridiani. *Geophys. Res. Lett.* 24, p. 2897-2900, 1997.

Kargel, J. S., and R. G. Strom, Ancient glaciation on Mars, *Geology* 20, p. 3-7, 1992.

Grant, J. A., and T. J. Parker 2002.

Parker, T. J., R. S. Saunders, and D. M. Schneeberger, 1989. Transitional Morphology in the West Deuteronilus Mensae Region of Mars: Implications for Modification of the Lowland/Upland Boundary. *Icarus* 82, 111-145.

Parker, T. J., D. S. Gorsline, R. S. Saunders, D. C. Pieri, and D. M. Schneeberger, 1993. Coastal Geomorphology of the Martian Northern Plains. *Journ. Geophys. Res.* 98, No. E6, p.11,061-11,078.

Parker, T. J., S. M. Clifford, and W. B. Banerdt. Argyre Planitia And The Mars Global Hydrologic Cycle. *Lunar and Planetary Science Conference – 31*, 2p., 2000.

Parker, T. J., 1989. Channels and valley networks associated with Argyre Planitia, Mars. *Lunar and Planet. Sci. - XX*, *Lunar and Planet. Inst.*, p. 826-827.

- Parker, T. J., 1994. Martian Paleolakes and Oceans, Ph.D. Dissertation, University of Southern California, 200p.
- Parker, T. J., 1997. Fluvial and lacustrine degradation of large highland basins during the Noachian. In Clifford, S. M., A. H. Treiman, H. E. Newsom, and J. D. Farmer, eds. Conference on Early mars: Geologic and Hydrologic Evolution, Physical and Chemical Environments, and the Implications for Life. LPI Contribution No. 916, Lunar and Planetary Institute, Houston, p. 65.
- Parker, T. J., and Currey, D. R., 2001. Extraterrestrial Coastal Geomorphology, *Geomorphology* 37, p. 303-328.
- Tanaka, K. L. and Scott, D. H. 1987. Geologic Map of the Polar Regions of Mars. Atlas of Mars, 1:15,000,000 Geologic Series, USGS Map I-1802-C.

STRATIGRAPHIC IMPLICATIONS OF THE RELAXATION OF TROUGHS AND SCARPS WITHIN THE MARTIAN NORTH POLAR LAYERED DEPOSITS. A. V. Pathare¹ and D. A. Paige², ¹California Institute of Technology (avp@gps.caltech.edu), ²University of California, Los Angeles (dap@mars.ucla.edu)

Introduction: Previously [1], we showed that the viscous relaxation of subsurface water ice in the North Polar Layered Deposits (NPLD) provides a much better fit than does surface sublimation to the key morphological observations of NPLD troughs and scarps. These include: the lack of latitudinal dependence of either the maximum surface slope or total depth of NPLD troughs; the correlation of maximum surface slope to total depth of NPLD scarps; the equatorward-facing/poleward-facing (EWF/PWF) slope asymmetry of opposing NPLD trough walls; and the presence of extremely steep NPLD scarps well above the angle of repose. Here, we argue that the stratigraphy of North PLD troughs and scarps is also more consistent with relaxation.

Trough Evolution: The results of both our sublimation modeling and relaxation simulations indicate that NPLD troughs are relatively young features [1]. For if NPLD troughs predate the last high obliquity epoch ($5 \text{ Ma} < t < 10 \text{ Ma}$), then neither EWF nor PWF walls experience a significant long-term sublimation advantage, which means that the observed trough slope asymmetry cannot be sustained by preferential sublimation of EWF walls. Moreover, trough closure relaxation times (to a depth of less than $d = 200 \text{ m}$) at high obliquities are much shorter than at present, due to increased subsurface temperatures. Thus we conclude that most North PLD troughs have probably formed within the last 5 Myr—most likely during the transitional period from high to low mean obliquity that Martian orbit models consistently place at $t \sim 4 \text{ Ma}$ [2,3].

The central question is: what mechanism has governed the subsequent evolution of North PLD troughs? More specifically, does the NPLD trough asymmetry somehow result from preferential sublimation of EWF walls during the last few Myr—despite the greatly reduced sublimation rates at lower obliquities? Or is the slope asymmetry produced by differential relaxation of EWF and PWF trough walls that arises from insolation-driven thermal variations? The strong morphological correlation of trough depth and slope, which is difficult to explain in terms of sublimation, is consistent with the predicted relaxation history of North PLD troughs [1]. Additional support for the relaxation hypothesis is provided by the observed stratigraphy of NPLD troughs.

Trough Stratigraphy: Fig. 1a shows a high-resolution MOC observation of a typical North PLD trough (the location of which is outlined in the wide-

angle context image of Fig. 1b). PLD troughs have been divided [4] into three main stratigraphic units: (1) Layered Terrain, expressed upon EWF trough slopes; (2) Banded Terrain, located on PWF trough walls; and (3) Smooth Terrain, which spans the regions between the troughs.

The EWF Layered Terrain are comprised of clearly delineated fine-scale laminae, most of which are relatively dark in appearance. The continued visibility of these layers implies active resurfacing by not only water ice sublimation but also eolian erosion—otherwise, a sublimation dust lag would be expected to form [5,6]. The wider layers of the intermediate-toned PWF Banded Terrain are much more irregular, and have been interpreted as representing the eroded “feather edges” of ice or dust layers deposited on PWF trough walls [4]. These two stratigraphic units provide the basis for the standard model of trough evolution in which water ice sublimed from the EWF Layered Terrain recondenses upon the PWF Banded Terrain, resulting in the poleward migration of the trough [4].

However, we argue that the relative thinness of the Banded Terrain actually indicates that deposition within troughs is insignificant. The diffuse Banded Terrain often appear to be translucent, exposing underlying fine-scale layers upon PWF trough walls that are continuous with their EWF Layered Terrain counterparts [4]. But deposition of a millimeter-thick layer should be more than sufficient to alter surface albedo and obscure the trough wall [7]. If we conservatively assume that the average thickness of the Banded Terrain is a full meter, then given that most present-day NPLD troughs likely formed about 4 Ma, the implied net deposition rate is only 0.25 microns per year—or about three orders of magnitude less than the MAWD-derived net NPLD sublimation rate of 0.19 mm/yr [1].

Undulations: The bright Smooth Terrain, which corresponds to the water ice surface of the North Permanent Cap (NPC), gradually transitions into the Layered Terrain (Fig. 1a), which is why the NPC is widely presumed to simply represent the uppermost layer of the North PLD [8]. Although the Smooth Terrain often appears to be featureless in summertime images (Fig. 1b), springtime observations such as Fig. 1c that highlight topography (due to the ubiquity of the seasonal CO₂ frost cap) reveal the presence of gentle wave-like undulations [4]. These shallow undulations typically have a vertical amplitude of 10-100 m, and are most prominent parallel to the equatorward (i.e., southern) edge of North PLD troughs [6].

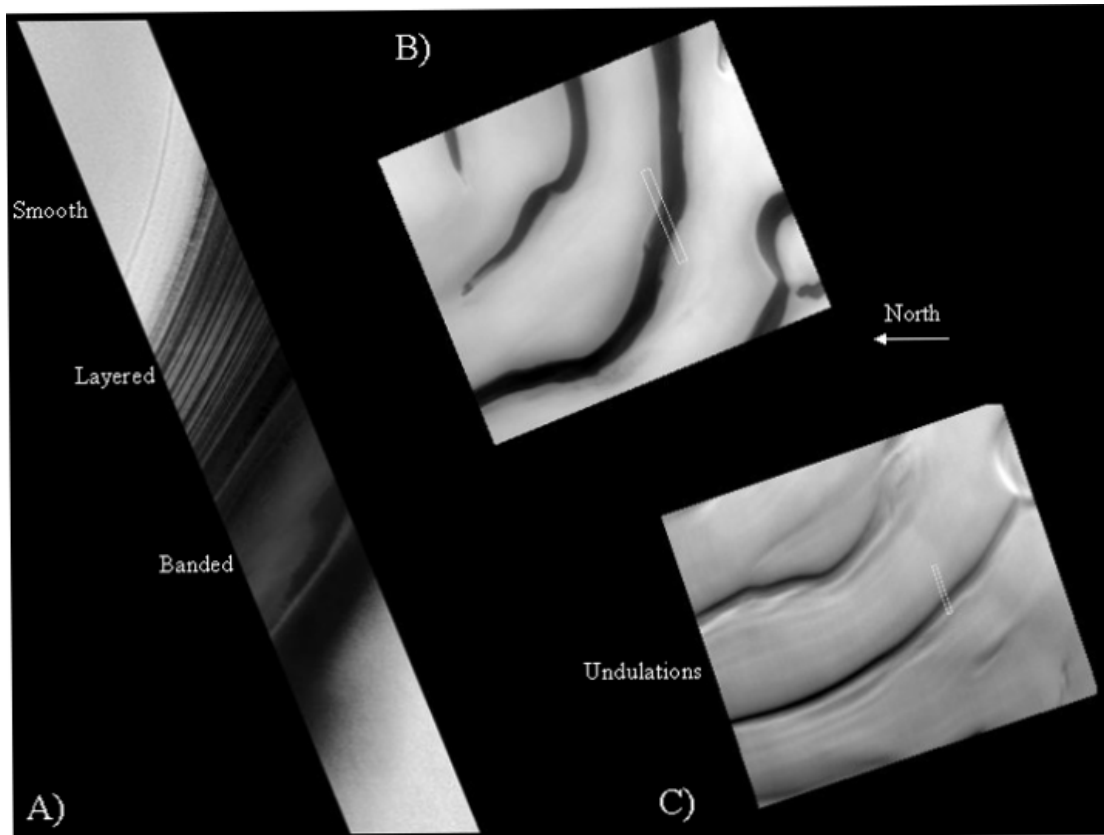


Figure 1 North PLD Trough Stratigraphy. MOC images (a) E01-01092: 87.0°N, 264.4°W, resolution = 13.0 m/pixel, size = 3.34 × 36.3 km, $L_s = 118^\circ$; (b) E01-01093: 87.4°N, 265.8°W, resolution = 274 m/pixel, size = 133 × 113 km, $L_s = 118^\circ$; (c) M18-00805: 86.7°N, 282.4°W, resolution = 272 m/pixel, size = 133 × 114 km, $L_s = 35^\circ$. Context for part (a) shown in part (b).

In the context of trough migration, the undulations are theorized to be “scars” representing the former positions of trough floors undergoing poleward retreat [4]. The main difficulty with this theory is that the troughs are currently substantially deeper than the undulations; hence, some mechanism must have increased the depth of the troughs while preserving the shallowness of the undulations, which given their proximity seems unlikely [6]. Alternatively, the undulations were formerly much deeper and have subsequently experienced massive infill. But the rate of trough deposition implied by the thin PWF Banded Terrain layers is much too low to raise deep trough floors by several hundred meters on Myr time scales.

However, our finite element simulations of North PLD troughs demonstrate that viscous relaxation can produce such rapid trough floor uplift, particularly at high obliquities [1]. Furthermore, our modeling indicates that troughs that have attained “closure” (defined for convenience as the time when $d < 200$ m) still retain a distinct V-shape which is similar in appearance

to the gentle trough-like morphology of undulations [6].

Therefore, we propose that undulations within the Smooth Terrain represent relict paleo-troughs that have experienced closure via viscous relaxation. Similarly, the slope asymmetry of present-day North PLD troughs is concordant with differential flow rates resulting from intra-trough thermal variations, which could either result from the expected slope dependence of surface temperature or from the generally lower albedo of EWF Layered Terrain relative to PWF Banded Terrain [1]. Thus we conclude that viscous relaxation is the resurfacing mechanism most consistent with both the stratigraphy and topography of NPLD troughs.

Scarp Evolution: Much like troughs, North PLD scarps exhibit a strong correlation between maximum slope and total depth, which is consistent with the predicted depth dependence of viscous relaxation. Our finite element modeling also indicates that the initial slope sensitivity of viscous relaxation can account for the presence of numerous extremely steep PLD scarps

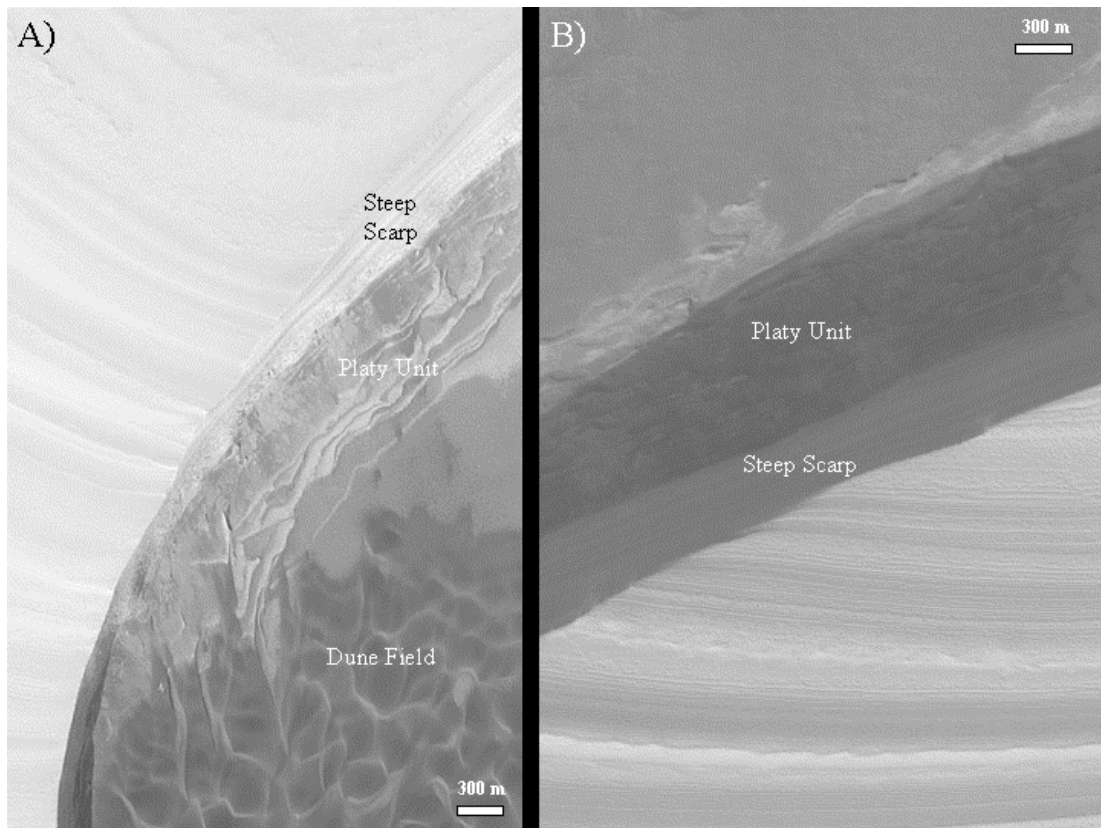


Figure 2 North PLD Scarp Stratigraphy. Portions of MOC NA images (a) E01-01773: 83.6°N, 242.0°W, resolution = 4.9 m/pixel; and (b) E02-01503: 85.4°N, 173.6°W, resolution = 3.2 m/pixel.

with surface slopes much greater than $\alpha = 40^\circ$ [9]. An alternative mechanism for oversteepening of scarps is eolian erosion of a basal layer [4,6]. The validity of these theories can be assessed by examining the stratigraphy of steep North PLD scarps, two of which are shown in the high-resolution MOC images of Fig. 2.

Scarp Stratigraphy has been divided [4,9] into three main units: (1) the Steep Scarp itself, which is often arcuate in shape and like EWF trough walls is comprised of finely Layered Terrain; (2) the Platy Unit located at the base of the scarp, which appears to consist of irregularly jumbled layers; and (3) nearby Dune Fields, which are often located in the vicinity of PLD scarps, whence they are most likely derived. One widespread interpretation of Fig. 2a is that the apparent formation of dunes from the Platy Unit leads to “creation of steep scarps as the sand is removed and the upper unit is undermined” [10].

However, we have two major objections to this conclusion. First of all, it is difficult to envision how scarp slopes so much greater than the angle of repose ($\alpha \gg 35^\circ$) can be stable in the presence of extensive eolian erosion [6]. Secondly, the basal undermining

hypothesis requires that the lower unit is less resistant to erosion than the overlying scarp; yet as seen in Fig. 2b, Platy Units generally extend outward by as much as a km from the base of the upper layers [9]. Thus Platy Units are clearly *more* resistant to erosion than the layered terrain of the Steep Scarps, which appear to have undergone extensive lateral retreat, most likely due to sublimation of water ice.

Basal Conditions: The presence of the basal Platy Units may also explain why the Steep Scarps appear to remain frozen at their base, which is an essential requirement for the long-term steepening predicted by our finite element scarp simulations [1]. For if the Platy Units are significantly rougher than the overlying scarps (as consistent with their apparent corrugation: Fig. 2a), then lateral advance of the scarp via basal sliding will be inhibited, particularly at the low subsurface temperatures characteristic of the NPLD. Of course, collapse of the overlying scarps may still occur, but the lack of observed taluses—either upon the Platy Units or just off the NPLD—at the $\alpha \sim 35^\circ$ angle of repose for unconsolidated material suggests that such collapse has not occurred. (Indeed, the presence

of dramatically steeper slopes is consistent with the $\alpha > 60^\circ$ angle of repose measured for snow avalanches composed of fresh crystalline water ice.)

Therefore, we propose that viscous relaxation is the most likely mechanism of steep scarp formation, as our finite element simulations yield maximum surface slopes well above the angle of repose for a variety of initial conditions [1]. Since subsurface flow also best explains the correlation of PLD scarp slope with depth, we conclude that viscous relaxation is consistent with both the stratigraphy and topography of NPLD scarps.

Recent NPLD Evolution: Almost all models of recent NPLD evolution presume that the EWF Layered Terrain (Fig. 1a) is actively sublimating, since its unobscured fine-scale layering clearly indicates a lack of present-day accumulation [4], and because the slope dependence of sublimation favors EWF trough walls at the current obliquity [1]. However, the relative importance of sublimation and condensation upon other units is more contentious.

The uniformitarian evolutionary hypothesis assumes that water ice sublimed from EWF Layered Terrain continually condenses upon both opposing PWF Banded Terrain and adjacent flat-lying Smooth Terrain, a pattern that results in the steady poleward migration of the trough [4]. The evidence for deposition upon the Banded Terrain mainly consists of that unit's characteristically wide and diffuse layers [4]—although as discussed above, the magnitude of such deposition is limited by the apparent thinness of these bands. As for the Smooth Terrain, analogy with terrestrial glaciers suggests that the bright whitish hue of this unit is indicative of accumulation, in contrast to the ablation implied by the darker Layered Terrain [11].

However, this simple albedo-based argument is stratigraphically inconsistent. For even though the PWF Banded Terrain is more favored for condensation than the flat-lying Smooth Terrain, the Banded Terrain generally has an albedo intermediate between that of the dark Layered Terrain and the bright Smooth Terrain (Fig. 1a). In other words, if the Smooth Terrain has a high albedo because it is accumulating fresh water ice, then why isn't the Banded Terrain at least as bright?

Therefore, we argue that the inter-trough Smooth Terrain is undergoing net sublimation, along with the EWF Layered Terrain. Moreover, the obliquity dependence of sublimation suggests that the PWF Banded Terrain may also be ablating. For example, our sublimation modeling predicts that the $\theta = 26.2^\circ$ summertime sublimation rate from a nominal $\alpha_e = -3.1^\circ$ NPLD surface (corresponding to the mean slope of PWF trough walls) is $E_{net} = 0.43$ mm/yr, which is

slightly *greater* than the present obliquity ($\theta = 25.2^\circ$) $E_{net} = 0.42$ mm/yr calculated for a nominal $\alpha_e = 5.4^\circ$ NPLD surface (characteristic of the mean slope of EWF trough walls). These results imply that opposing trough walls are in different sublimation/condensation regimes for a relatively narrow obliquity window (the actual width of which depends upon the uncertain orbital modulation of wintertime H₂O recondensation). Hence we suspect that the diffuse bands observed upon PWF trough walls result from deposition at lower obliquities, and that over the probable 3-5 Myr lifetimes of North PLD troughs, the PWF Banded Terrain undergoes net sublimation.

Consequently, we suggest that long-term deposition of H₂O does not occur anywhere in the vicinity of troughs. Instead, we propose that net condensation of water ice is restricted to the very center of the North PLD (where troughs are absent) via the "vacuum effect" associated with repeated H₂O recondensation within the retreating seasonal CO₂ cap. However, this scenario of widespread ablation throughout the outer NPLD and focused accumulation within the inner NPLD raises long-term stability concerns, since the MAWD-derived average North PLD sublimation rate of $E_{net} = 0.19$ mm/yr is fast enough to transfer a $Z = 1$ km thick layer from the outer to the inner NPLD in a little over 5 Myr. Thus in order to prevent massive thickening near the pole, some process must be redistributing material back to the margins.

Our modeling implies that glacial flow is the most likely mechanism of maintaining mass balance within the North PLD. For not only do our sublimation calculations indicate that the NPLD is divided into ablation and accumulation zones (much like terrestrial glaciers), but our finite element relaxation modeling clearly demonstrates that the PLD consist of deformable ice—which is a fundamental prerequisite for glacial flow. Therefore, we conclude that flow processes not only control the relaxation history of mid-sized features such as troughs and scarps, but also govern the large-scale evolution of the entire North PLD.

References: [1] Pathare A. V. and Paige D. A. (2003) *LPS XXXIV*, Abstract #2051. [2] Ward W. R. and Rudy D. J. (1991) *Icarus*, 94, 160-164. [3] Touma J. and Wisdom J. (1993) *Science*, 259, 1151-1154. [4] Howard A. D. et al. (1982) *Icarus*, 50, 161-215. [5] Hofstadter M. D. and Murray B. C. (1990) *Icarus*, 84, 352-361. [6] Howard A. D. (2000) *Icarus*, 144, 267-288. [7] Bass D. S. et al. (2000) *Icarus*, 144, 382-396. [8] Clifford S. et al. (2000) *Icarus*, 144, 210-242. [9] Byrne S. and Murray B. C. (2002) *JGR*, 107 (E6), 11-1. [10] Malin M. C. et al. (2002) Release # MOC2-311. [11] Fisher D. A. (2000) *Icarus*, 144, 329-352.

TESTING THE PSEUDOCRATER HYPOTHESIS. M. C. Payne¹ and J. D. Farmer¹, ¹Arizona State University (Department of Geological Sciences, PO Box 1404, Tempe, AZ 85287, mcpayne@asu.edu, jfarmer@asu.edu)

Introduction: In a regional study of the margin of the north polar cap, a field of coniform features was observed in the Olympia Planitia region and hypothesized to be a pseudocrater field (Figure 1). Volcanic features located at the margin of a polar cap has great significance for astrobiology. Such interactions could provide potential shallow subsurface habitable zones of liquid meltwater, as well as a mechanism for transporting a subsurface biota into near-surface environments via convecting hydrothermal systems. Such a biota, or prebiotic organic chemistry, could be subsequently cryopreserved in shallow polar ground ice formed as such systems cooled and died. In this study, a number of methods were employed to test the pseudocrater hypothesis, including feature profiling (using MOLA data), geomorphic measurements (e.g. crater diameter/ cone diameter ratios), nearest neighbor analysis, and comparisons to potential terrestrial analogs. Candidate analog terrestrial landforms studied included Icelandic pseudocraters, cinder cones, shield volcanoes, maar craters, pingos, and hummocky moraine. Comparisons were also made with martian rampart craters, and features previously interpreted as martian pseudocraters.

Description of Knobby Terrain: On the margin of the remnant ice cap of the north pole, centered at approximately 75°N latitude, 216°W longitude, lies a region of partially ice-covered hummocky terrain. The knobby topography covers an extensive region marginal to the remnant north polar cap and extending south to ~70° N latitude. Portions of this knobby terrain are visible in Viking image 063B21 (Figure 1). The knobs have very low relief, although central craters are present at the summits of many of the larger features. The knobs sit on pedestal-like surfaces that are raised above the surrounding polar plains. Elevation measurements made using a Digital Elevation Model (DEM) (constructed from MOLA data) indicate that the bases of the knobs are raised on average, 5-10 m above the surrounding terrain. Associated linear features may be fissure-ridges.

As previously mentioned, the knobs appear to be roughly coniform in nature, many of the larger forms having summit craters of circular to elliptical form. Poor resolution may account for the seeming absence of central craters in the smaller knobs.

Resolution played an important role in the interpretations of the features. In general, the enhanced resolution (~58 m/pixel) of the Viking image for the area

proved more helpful than the DEM, which had a spatial resolution of ~230 m/pixel.

Comparisons with Analog Landforms: A number of volcanic, as well as cold climate landforms, were proposed as potential analogs for the field of coniform features at the study site. Methods for the analysis of these features were adapted from previous authors [1-4]. A brief overview of the analysis of the observed coniform features and comparisons with potential analog landforms follows.

Rampart craters. Figure 2 compares MOLA profiles of two rampart craters present on the nearby northern plains of Mars near the study site, with a profile of Meteor Crater (a small terrestrial impact crater), and the knobby features at the study site. There are clear profile differences observed between each of these features. A nearest neighbor analysis of the knobby features yielded a random distribution expected for impact craters, but the geomorphology of these features, as noted above, suggests a different origin.

Volcanoes. The random distribution pattern for the knobby features, established through nearest neighbor analysis, is consistent with a volcanic origin, as there is no reason, *a priori*, to assume that the conduits from a magma body should organize themselves in a systematic (non-random) pattern. In MOLA profiles, slopes of the knobby features range from 0.01 to 0.02. Comparable terrestrial low shield volcanoes, such as Sandfell volcano in Iceland, have similar slopes. However, the average crater diameter/cone diameter ratio for the knobby features is 0.39, which is most similar to the value for terrestrial cinder cones (~0.40) and not shield volcanoes (0.06-0.12) [1]. Indeed, a comparison of the Martian knobby features with a variety of terrestrial volcanic constructs (including spatter cones, cinder cones, pseudocraters, maars, and shield volcanoes) and small coniform features on the Moon [1], showed that, in general, the features compare most closely to terrestrial maar craters and cinder cones. We note that features in the region of the northern plains in close proximity to the polar cap were previously compared to terrestrial shield volcanoes [2]. However, without a detailed knowledge of the scaling factors used to correct terrestrial features for differences in martian gravity, it was not possible in the present study to reproduce those analysis methods in this work. It is noted that the reduced martian gravity and atmospheric density has a substantial effect on the morphometry of martian pyroclastic cones [1]. All other factors being equal, the lower gravity and atmospheric density of

Mars produce pyroclastic eruption features that are wider and lower in relief than their terrestrial counterparts [3,5].

The crater diameter/cone diameter ratio of the coniform features is ~ 0.40 - 0.60 . These values overlap with values for both terrestrial pyroclastic features [1], and martian rampart craters. Hence it seems clear that this ratio cannot be regarded as diagnostic. While some of the knobby features observed in Figure 1 are similar to terrestrial cinder cones, further modeling is needed to understand the differences between terrestrial cinder cone profiles and those for cones formed under the low gravity and thin atmospheric conditions of Mars. Furthermore, similar knobby features were observed over a vast area, stretching from the margin of the remnant ice cap, extending south to $\sim 70^\circ$ N latitude. This distribution pattern is hard to explain with a volcanic hypothesis.

Maar craters. Almost half of the data points for the coniform features observed at the study site compared well with terrestrial maar craters [1]. Slopes of some terrestrial maar craters measured on DEMs ranged from 0.012 to 0.053; however, diameters over this range of slopes varied widely from a few hundred meters to over six kilometers. Maar crater morphologies could be expected to have an even broader morphological range on Mars, due to the effects of lower gravity and thinner atmosphere on the trajectory of material excavated by the explosion, as well as the depth of point source phreatic explosions. Therefore, even though the profiles of the knobby features observed in the study site (Figure 1) do not show good agreement with terrestrial maar crater profiles, this interpretation is difficult to rule out *a priori*. Again, as with the volcano hypothesis previously discussed, a maar crater hypothesis is hard to justify, given the broad distribution of the knobby features over the northern plains.

Pseudocraters. Pseudocraters are rootless pyroclastic cones formed where lava flows over wet or icy ground, triggering phreatic eruptions that produce fields of small scoria cones on the surface of a lava flow. Many authors have postulated these features to be terrestrial analogs for landforms observed on Mars [3-7]. A variety of pseudocrater types have been described in Iceland, adjacent to inland lakes and on glacial outwash plains. The morphologies of pseudocraters are thought to depend on the abundance of water during their formation [5]. Many authors have used the crater diameter/cone diameter ratio to identify potential martian pseudocraters [1, 3-5]. We used size-frequency histograms to compare the knobby features observed at Olympia Planitia (this study), with martian and terrestrial pseudocraters identified by previous authors [3-5]. *Wood's* [1] average value for the crater

diameter/cone diameter ratio for terrestrial pseudocraters (0.42) is slightly higher than the average value measured for the features observed in this work (~ 0.39). In addition, no data points for the knobby features in the present study fell within the range for terrestrial pseudocraters reported by previous authors [3, 4]. However, a significant overlap was observed with previously reported martian pseudocraters [4] (see Figure 3). Specifically, we note that the smallest features observed in the present study area are larger than any pseudocraters identified by *Greeley and Fagents* [3] (Figure 3). At the other end of the distribution, features in the study region with diameters larger than the Martian pseudocraters proposed by *Frey and Jarosewich* [4] (see Figure 3) were re-interpreted in the present study, to be rampart craters (see feature profiles 21 and 22, Figure 2). While examples of pseudocraters as large as the knob-like features observed in the Olympia Planitia study site have not been reported in the previous literature, authors have demonstrated that the reduced gravity and atmospheric density on Mars could produce martian pseudocraters many times larger than terrestrial pseudocraters (although lower in relief) [3, 5]. (Similar arguments were made previously for cinder cones). Furthermore, it has been shown that, compared with Earth, far less ice is needed on Mars to create terrestrial-sized pseudocraters [3,5]. Hence, it may be inferred that in the north polar region of Mars, where ice is abundant, pseudocraters could grow to much larger proportions than achievable on Earth.

Pseudocraters develop on the surface of a single lava flow as it cools, and their distribution pattern is governed by heat loss. Hence, pseudocraters and related features (e.g. tumuli on ash flows) may be expected to have a somewhat uniform, to systematically varying distribution, and not the random pattern observed in a nearest neighbor analysis of the knobby features in the present study. And similar to conclusions for a cinder cone or maar crater origins, the broad distribution of the features, along the remnant ice cap margin, extending over a broad region of the northern plains, is hard to explain by a pseudocrater hypothesis. We therefore dismiss the pseudocrater hypothesis as problematic.

Pingos. Pingos are terrestrial landforms that form in cold climates where a freezing front advances on a talik (an unfrozen lens of water existing in permafrost), forcing the water upward and deforming the overlying bedrock into a dome-like feature. Pingos have a conical to elliptical form, often with a central crater-like depression. Pingos were rejected as a possible analog for the features observed at the study site because they are unlikely to exceed 1 km in diameter, even under martian conditions (S. D. Gurney, Univer-

sity of Reading, personal communication, 2002). However, should a dense eutectic brine be substituted for pure water on Mars, it might be possible to create large pingos (> 1 km in diameter), similar to those found in the study area [8, 9]. Terrestrial pingos in open aquifer systems often form in clusters [10]. However, a new pingo is more likely to form in the footprint of an older, collapsing pingo, creating overlapping features. This process results in features quite different from the coniform features observed in our study area [10]. Furthermore, terrestrial pingos are not known to exist in dense groupings as numerous and as extensive as the knob-like features observed in the study area (S. D. Gurney, University of Reading, personal communication, 2002). Lastly, pingos often display radial cracking, with fractures extending from their central depression to the outer flanks of the cone. Radial cracking was not observed in any of the knob-like features observed at the study site, nor was such a pattern evident in MOLA data, although that may be beyond the limits of detectability with those data. As with terrestrial pseudocraters, terrestrial pingos are too small to appear on topographic maps, so that comparable feature profiles were unavailable. However, even if the knob-like features observed at the study site are pingos, direct, same-scale comparisons with terrestrial pingo profiles, may be irrelevant because the processes necessary to form such large pingos do not exist on Earth. Although the knob-like features observed at the Olympia Planitia study site are not interpreted to be pingos, these features are of interest to astrobiology because they form where subsurface liquid water rises to the surface and freezes.

Hummocky moraine. On Earth, ice loading along stagnant glacial margins has been postulated to deform fine-grained till into hummocks, depressions, and ridges [11, 12]. These subglacial till deformation features, called "hummocky moraine," are prevalent along the border of Canada with the United States, where they formed along the margin of the Laurentide Ice Sheet during the Pleistocene [e.g. 11, 12]. Hummocky moraine covers vast areas, occurring in broad belts tens of kilometers wide [12]. Hummocks are typically 1-50 m high, 25-300 m wide, and have slopes ranging from 1°-25° [13]. They are often closely spaced, although their distribution is chaotic [11, 12]. Previous models to explain the origin of hummocks emphasized a supraglacial origin. However, hummocks have been found to contain cores of fine-grained till [11-14]. Therefore, recent work postulates a subglacial pressing mechanism based on the liquefaction of tillites during glacial loading [11, 12]. Ice-loading and deformation of subglacial till can produce a wide variety of hummocky forms, including both flat-topped mounds and mounds with central depressions (also known as

doughnuts). The subglacial processes responsible for forming hummocky moraine involve partial liquefaction of the underlying till during glacial stagnation and recession. Such features may apparently also form during basal melting of a glacier [12], or erosionally during catastrophic, jökulhlaup-type glacial outflow events [13, 14]. The morphometry of hummocky moraine shows good agreement with the knobby features observed at the Olympia Planitia study site. Mound-shaped hummocky moraine can occur in a wide variety of sizes and morphologies, but are typically low-relief coniform features. Hummocks within the same region may or may not have a central depression. The mounds comprising hummocky moraine have a random distribution, and extend over broad regions, generally parallel to glacial margins of formerly glaciated terrains. Thus, a hummocky moraine interpretation satisfactorily explains the wide distribution of similar knobby features present on the northern plains of Mars. As argued for pingos, the replacement of pure liquid water by dense eutectic brines on Mars [8, 9] may produce features much larger than those created on Earth. In any case, subglacial, water-rich environments are of great interest to astrobiology. Because hummocky moraine forms along glacial margins during recessional intervals, the hummocky features observed in the study area are probably younger than similar features located further south and therefore would be more likely to preserve subsurface zones of liquid water. And if the knob-like features observed in this study are hummocky moraine features, their present distribution reveals the former extent of the martian north polar cap.

Conclusions: Almost certainly, the region of study includes a mixture of geomorphic features, having several different origins. Some knobs may even be polygenetic, having been initiated by impact cratering or volcanic events and subsequently modified by glacial ice. For most of the knobby features observed at the Olympia Planitia study site, however, a hummocky moraine hypothesis is preferred. This explanation accounts for not only the morphology of the landforms, but also their distribution as well. Specifically, the hummocky moraine hypothesis provides a satisfactory explanation for the existence of similar landforms at lower latitudes, and is consistent with the recent suggestion of large amounts of ground ice persisting at lower latitudes during periods of higher obliquity at Mars [e.g. 15-17].

Astrobiological Significance: Within the study area, habitable environments of subsurface liquid water could have been created in a variety of ways, including the following: shallow hydrothermal systems associated with pseudocraters, deeper hydrothermal systems associated with centralized volcanic eruptions

and impact craters, upwelling of shallow groundwater during pingo formation, and subglacial melting associated with the formation of hummocky moraine. All of these processes provide effective ways for creating: 1) shallow subsurface zones of liquid water and 2) mechanisms for transporting a subsurface biology near surface environment cryosphere, where it could be sequestered and cryopreserved in ground ice. For these reasons, the region encompassed by the study site at Olympia Planitia is considered an important astrobiological target for future landed missions.

References: [1] Wood, C. A. (1979), *LPS X*, 2815-2840. [2] Garvin, J. B. et al. (2000) *Icarus*, 145, 648-652. [3] Greeley, R. and Fagents S. A. (2001) *JGR.*, 106, 20,527-20,546. [4] Frey, H. and Jarosewich, M., (1982) *JGR*, 87, 9867-9879. [5] Fagents, S. A. et al. (2002) in *Volcano-Ice Interaction on Earth and Mars*, Smellie, J. L. and Chapman, M. G. (eds), 295-317. [6] Frey, H. et al. (1979) *JGR.*, 84, 8075-8086. [7] Lanagan, P. D. et al. (2001) *GRL*, 28, 2365-2367. [8] Kuz'min, R. O. and Zabalueva E. V. (1998) *Solar System Res.*, 32, 187-197. [9] Knauth, L. P. and Burt D. M. (2002) *Icarus*, 158, 267-271. [10] Gurney, S. D. (1998) *Progress in Physical Geography*, 22, 3, 307-324. [11] Eyles, N. et al. (1999) *Sediment. Geol.*, 123, 163-174. [12] Boone, S. J. and Eyles, N. (2001) *Geomorphology*, 38, 109-124. [13] Munro, M. and Shaw, J. (1997) *Geology*, 25, 1027-1030. [14] Munro, M. et al. (1999) *Sediment. Geol.*, 129, 165-168. [15] Jakosky, B. M. and Carr, M. A. (1985) *Nature*, 315, 559-561. [16] Jakosky, B. M. et al. (1995) *JGR*, 100, 1579-1584. [17] Mellon, M. T. and Jakosky B. M. (1995) *JGR*, 100, 11,781-11,799.

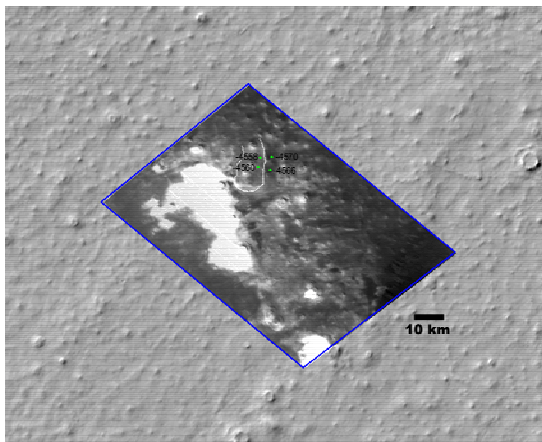


Figure 1: Viking image 063B21, in polar stereographic projection, overlain on the hill-shaded DEM. This image shows that some of the knob-like features sit on elevated platforms or pedestals. The white line

denotes the edge of the lobe of material upon which three knob-like features sit. Point elevation values were compared on either side of this boundary and showed an elevation difference of ~10 m.

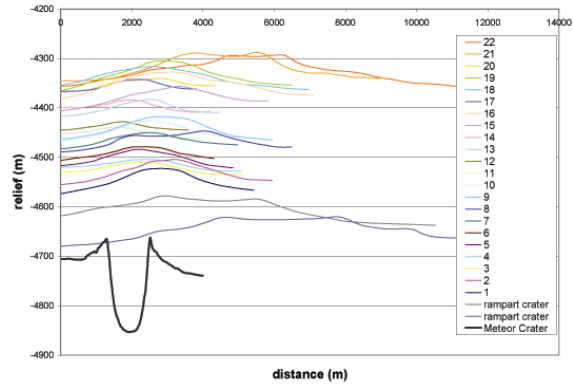


Figure 2: Profiles of 22 of the knob-like features observed in Viking image 063B21. Profiles of two northern plains rampart craters and Meteor Crater (a terrestrial impact crater) are also included for comparative purposes. Features 22, 21, and 8 appear to be in relatively good agreement with the rampart craters. No martian feature sampled here seems to correspond to the terrestrial impact crater, although ejecta trajectories on Mars would produce broader and lower relief features due to lower gravity and thinner atmosphere. $VE = 13.8$.

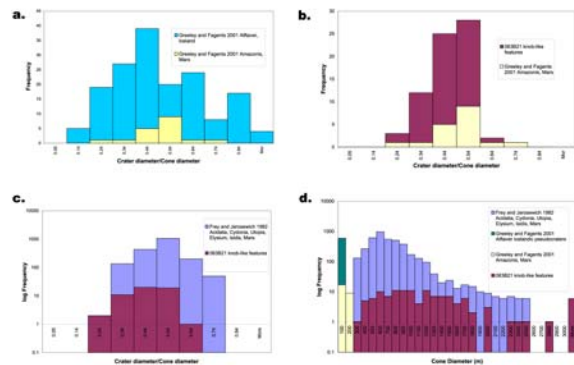


Figure 3: Histograms of crater diameter/Cone diameter (a-c) compare the knob-like features observed in Viking image 063B21 and pseudocraters identified by previous authors (b&c). (c) Histogram comparing proposed martian pseudocraters with Icelandic pseudocraters from Greeley and Fagents (2001). (d) Histogram showing the overlap in size between the knob-like features in Viking image 063B21 and the martian pseudocraters proposed by Frey and Jarosewich (1982). Note also the lack of overlap between the 063B21 features and either the martian or terrestrial pseudocraters identified by Greeley and Fagents (2001).

VISCOUS FLOW OF ICE-RICH CRATER FILL DEPOSITS AND PERIODIC FORMATION OF PROTALUS RAMPARTS: A CLIMATE RECORD?

J. T. Perron¹, A. D. Howard² and W. E. Dietrich¹,
¹Department of Earth and Planetary Science, University of California, Berkeley, CA 94720, per-
 ron@eps.berkeley.edu, ²Department of Environmental Sciences, University of Virginia, Charlottesville, VA 22904.

Introduction: Howard [1] has argued that the arcuate ridges of debris at or near the base of pole-facing crater walls at intermediate southern latitudes on Mars are analogous to terrestrial protalus ramparts, and that they formed at the margins of volatile-rich deposits mantling the crater walls. The presence of multiple generations of relatively undeformed ramparts on crater floors (Figure 1) suggests the advection of a rigid surface layer over deep deposits that fill the crater and are undergoing ductile deformation. Comparison of the cross-sections of these craters with those of fresh craters indicates the presence of several hundred meters of deposits, and MOLA profiles show that the crater floors slope in the apparent flow direction.

The observation that there is some regularity to the spacing of the ramparts (Figure 1) suggests that they formed in response to quasi-periodic climate changes. We use measured crater floor slopes and spatial relationships of ramparts, inferred fill deposit thicknesses, and ice flow laws to estimate the elapsed time between rampart formation events.

Flow model: We assume that ramparts are advected across crater floors by internal deformation of water ice-rich deposits filling the craters. By measuring the spacing between ramparts and estimating the surface velocity of the crater fill deposits, we can calculate the time elapsed between the creation of ramparts. The vertical velocity gradient $-du/dz$ in a body of ice deforming under its own weight is given by the shear strain rate

$$\dot{\gamma} = A \exp(-Q/R_G T) \tau^n \quad (1)$$

where A and n are constants, Q is the activation energy for ice creep, R_G is the ideal gas constant ($8.3143 \text{ J mol}^{-1} \text{ K}^{-1}$), T is temperature and τ is shear stress. Equation (1) describes the temperature-dependent, non-Newtonian rheology of ice, and is supported by many field and laboratory observations [2]. The driving shear stress is supplied by the horizontal component of the pressure gradient in the ice,

$$\tau = \rho g z \sin \alpha \quad (2)$$

in which g is gravitational acceleration (3.72 m s^{-2}), ρ is the bulk density of the ice-rich deposits, and α is the surface slope (in this case, the slope of the crater floor).

Substituting (2) into (1), integrating from h , the thickness of the crater fill deposit, to z , and evaluating the resulting expression at $z = 0$ gives the surface velocity of the ice. We must also account for the flow effects of the rock fraction of the crater fill deposits. Since only the ice within the fill deposits deforms, the bulk strain rate, and hence the surface velocity, must be reduced by a factor of $(1-\phi)$, where ϕ is the volume fraction of particulates. Experiments by Durham et al. [3] at $\sim 50 \text{ Mpa}$ show that volume fractions of silicate particulates above 10% increase the steady-state strength of ice by an amount that is greater than this expected geometric effect; however, it is not clear that the same behavior would occur at the low stresses found in thin bodies of ice.



Figure 1. Detail of MOC image E0200485. Section of a crater floor showing multiple sets of relict ramparts that have been advected toward the southern wall of the crater. The apparent right-lateral fault (F) suggests brittle deformation of a rigid surface layer underlain by deforming deposits.

The values of A , n and Q depend on the mechanism of ice deformation, which varies with the magnitude of the driving stress. Laboratory experiments by Goldsby and Kohlstedt [4] show that, at $\tau \sim 100$ kPa, sliding along grain boundaries ($n = 1.8$) dominates over dislocation creep. Following Nye [5], extrapolating the flow law of Goldsby and Kohlstedt to a grain size of 1 mm gives $A = 4.6 \times 10^{-9} \text{ Pa}^{-n} \text{ s}^{-1}$ and $Q = 49 \text{ kJ mol}^{-1}$. Other values adopted are $\phi = 0.3$, $\rho_{ice} = 920 \text{ kg m}^{-3}$ and $\rho_{rock} = 2800 \text{ kg m}^{-3}$. We assume a constant, uniform temperature throughout the ice; the effect of the thermal gradient is negligible for a deposit thickness of only a few hundred meters.

Periodic rampart formation: We measured the spacing between rampart crests in MOC images of seven craters with multiple, well-defined sets of ramparts. We then used MOLA profiles to measure the N-S slope of the crater floor and compared the crater profiles with the characteristic shape of fresh craters to estimate the central thickness of crater fill deposits [6]. Because fill thickness decreases toward the wall of the crater, we use half the central thickness as a representative value of h for each crater. Figure 2 shows the dependence of surface flow velocity on h for the measured range of crater floor slopes.

Dividing the mean rampart spacing by the surface velocity, we obtained an estimate of the time elapsed between rampart creation events for each crater. Table 1 lists our measured values and the estimated time scales for temperatures ranging from 190K to 220K. For a given temperature, the different craters yield times that are generally of the same order of magnitude. The sensitivity of ice viscosity to temperature makes it difficult to settle on a single time scale, but for the 30-degree range in Table 1, our estimates suggest that rampart formation events are relatively frequent, separated by at least 100 kyr and possibly as much as 30 Myr. The time scales for major variations in orbital parameters such as obliquity and precession

fall at the lower end of this range [7]. If ramparts have been advected across crater floors by the flow of ice-rich crater fill deposits, they may record the timing of particularly large, orbitally-driven climatic events.

References: [1] Howard, A.D. (2003) *LPSC XXXIV*, Abstract #1065. [2] Paterson, W.S.B (1994), *The Physics of Glaciers*. [3] Durham, W.B, S.H. Kirby and L.A. Stern (1992) *JGR*, 102, 16283-16302. [4] Goldsby, D.L. and D.L. Kohlstedt (1997) *Scripta Materialia*, 37, 1399-1406. [5] Nye, J.F. (2000) *J. Glac.*, 46, 438-444. [6] Garvin, J.B. et al. (2002) *LPSC XXXIII*, Abstract #1255. [7] Ward, W.R. (1992) in *Mars*, ed. H.H. Kiefer et al., 298-320.

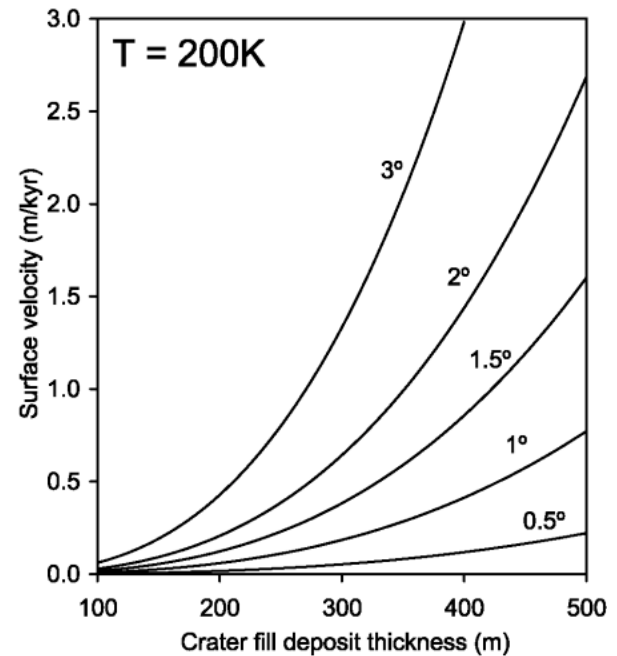


Figure 2. Predicted surface flow velocity of crater floor deposits as a function of crater fill deposit thickness with $T = 200\text{K}$. Curves for crater floor slopes from 0.5° to 3° are shown.

W Longitude/ S Latitude	Crater floor slope ($^\circ$)	Deposit thickness (m)	Number of ramparts	Rampart spacing (m) (mean \pm s.e.)	Time between rampart formation (kyr)		
					T=190K	T=205K	T=220K
157.57 / 39.65	2.17	479	3	342 ± 10	4057	419	59
166.25 / 39.06	2.72	270	2	259 ± 6	10257	1060	149
155.59 / 40.54	2.98	192	9	376 ± 13	32533	3362	474
171.92 / 42.79	0.51	488	8	161 ± 4	24712	2554	360
194.95 / 35.55	2.61	332	2	286 ± 22	6826	705	99
158.93 / 39.16	0.65	337	5	291 ± 10	80579	8328	1173
162.05 / 43.29	2.67	205	4	361 ± 23	31786	3285	463

Table 1. Estimated time scale between rampart formation events for temperatures ranging from 190K to 220K

NOACHIAN EVOLUTION OF MARS. R. J. Phillips¹, C. L. Johnson², B. M. Hynek¹, and B. M. Jakosky³
¹McDonnell Center for the Space Sciences and Department of Earth and Planetary Sciences, Washington University (Box 1169, One Brookings Drive, St. Louis, MO 63130; phillips@wustite.wustl.edu). ²Institute for Geophysics and Planetary Physics, Scripps Institution of Oceanography (9500 Gilman Drive, La Jolla, CA 92093; johnson@igpp.ucsd.edu). ³Laboratory for Atmospheric and Space Physics, University of Colorado (Boulder, CO 80309; bruce.jakosky@lasp.colorado.edu).

Introduction: The Noachian era on Mars is distinguished by the development of the Tharsis rise and the widespread creation of terrain types that likely required the involvement of running water. Here we review both aspects as well as possible interrelationships between Tharsis evolution and global geomorphic signals of fluvial activity.

Origin and Evolution of Tharsis: Following the development of the global crustal dichotomy, the tectonic and volcanic history of Noachian Mars was dominated by the development of the Tharsis rise. The construction of Tharsis was largely complete by the end of the Noachian [1, 2, 3] and upwards of 3×10^8 km³ of magmatic material may have been involved [1], equivalent to a global average thickness of 2 km. The volatiles associated with Tharsis magmas may have perturbed the climate in a significant way. Tharsis deformed the global lithospheric shell and induced major fault structures across the western hemisphere. The global warping of the lithosphere strongly influenced the orientations of many subsequent valley networks.

There have been a number of competing models for the origin of the Tharsis rise. Models employing a plume origin of Tharsis were proposed early [4, 5]. A long-standing issue with such models is the difficulty of numerically creating a single large plume (or two, if Elysium is considered). A single-plume structure might be generated in conjunction with the spinel to post-spinel endothermic phase change deep in the mantle [6,7], although the existence of a pressure sufficiently high for the phase change is questionable.

The major alternative to a plume model proposes that Tharsis is a region of weak (thin) lithosphere early in martian history, favoring localization of intrusive and extrusive magmatism [8]. Conceptually, heating associated with magmatism maintains a thin lithosphere in this passive model. Compensation of the load is isostatic early in Tharsis history, and flexural later due to thickening of the lithosphere.

Both types of models require buoyant uplift of the lithosphere, as does a third type of model that requires a low-density melt residuum in the upper mantle [9]. The passive model must maintain a hot, thus positively buoyant, upper mantle in order to maintain a thin lithosphere. Evidence for uplift is provided by circumferen-

tial graben in the Claritas Fossae region, first noted in [9], and supported by analyses [10] of more recent tectonic mapping [11].

Evidence for a mantle buoyant component in the creation of Tharsis might be found in a residual positive buoyancy in the present-day interior structure. Buoyancy structures due to plumes presently do not contribute more than 10% to the Tharsis geoid when considering the viscoelastic rheology of the mantle [12]. The consideration of simultaneous top (lithospheric) loading and bottom (mantle buoyancy) loading when constrained by the degrees 2 and 3 geoid-to-topography ratios indicates that a thermal plume could account for < 15% of the geoid and < 25% of the topography [13]. This then does not rule out a mantle plume (or more generally a mantle buoyant) contribution to the origin of Tharsis, but indicates that presently lithospheric loading, presumably by igneous masses, accounts for the majority of the geoid and topography. Further, pervasive Noachian tectonic structures can be explained by lithospheric loading models using the present-day high-fidelity geoid and topography fields obtained by MGS [2]. This indicates that the types and distributions of the loads have changed little since the end of the Noachian, i.e., any plume component was no longer dominant by then. The simplest explanation for the orientation and structural type of the majority of tectonic features in the western hemisphere remains that of flexural/membrane loading of a thin elastic spherical shell [2]. However, dike emplacement could have had an important influence on tectonic fabric [14, 15].

Recent analysis of magnetic field data indicates crustal anomalies high on the Tharsis rise, with the strongest anomalies associated with Noachian terrain and lesser anomalies associated with younger volcanic areas [10]. The Hesperian and Amazonian volcanics on Tharsis are a thin veneer (< a few km) covering a Noachian substrate [1], so it is likely the magnetic anomalies there are also Noachian in origin. There are two possibilities for the origin of the high-elevation magnetic anomalies: (i) Magnetic anomalies in uplifted Noachian basement survived, which is plausible [16]. (ii) The magnetization was acquired as Tharsis magmas themselves cooled through the Curie temperature, and this magnetization subsequently survived erasure by

later igneous activity. We note that it is possible that the uplift inferred structurally at Tharsis could have taken place merely by crustal thickening due to igneous intrusion, regardless of the nature of the origin of upper mantle buoyancy.

Thus, with the aid of MGS data, we can draw reasonably firm conclusions that (i) There is a strong igneous constructional component to Tharsis that was nearly complete by the end of the Noachian, though lesser volcanism in the Hesperian and Amazonian indicates the continued presence of a warm, though diminished mantle source. (ii) An upper mantle buoyancy anomaly existed beneath Tharsis as it was forming. This anomaly had a large thermal component, which was responsible for extensive partial melting that created the bulk of the Tharsis melts. (iii) It is not possible at this time to assign the relative proportions of active and passive components to this buoyancy.

Noachian Fluvial Geomorphology: The formation of ubiquitous valley networks and extensive erosion during periods in the Noachian has led to the idea that fluvial erosion was an important process on Noachian Mars [17]. However, the occurrence of olivine, highly weatherable in the presence of water, and the lack of any significant accumulations of carbonates at the surface [18] argues against long-standing bodies of water during Noachian times. Additionally, climate models cannot produce, to the community's overall satisfaction, clement conditions for Noachian Mars [19, 20].

Recent analyses of MGS data show that valley network geomorphology is much more Earth-like than previously thought in terms of stream order and density [21]. Figure 1 shows an example region in Arabia Terra, where the valley system is 6th order and the drainage density is $6.5 \times 10^{-2} \text{ km}^{-1}$. Measured at roughly the same resolution, this drainage density approaches the low end of terrestrial values [22]. Moreover, many of the valleys reach up to drainage divides.

MGS and earlier data sets provide information on widespread Noachian erosion [23, 24, 25]. Documented in the Tharsis trough [1] from the Margaritifer Sinus region to northwestern Arabia Terra is a dramatic late Noachian denudation of the landscape that left behind inliers containing valleys predating the denudation [25] (Figure 2). It is estimated that $\sim 5 \times 10^6 \text{ km}^3$ of material was stripped away, and water is the most likely agent of erosion. Earlier erosion events, chiefly documented by crater degradation [23], indicate that erosion was an on-going, though possibly episodic, phenomenon throughout much of the Noachian.

Geomorphic indications that sapping was a dominant process in valley network formation does not ob-

viate the need for precipitation, particularly as valleys extend to drainage divides. Infiltration of highly permeable near-surface stratigraphy and recharging of ground water systems may have enabled long-term sapping [26, 27].

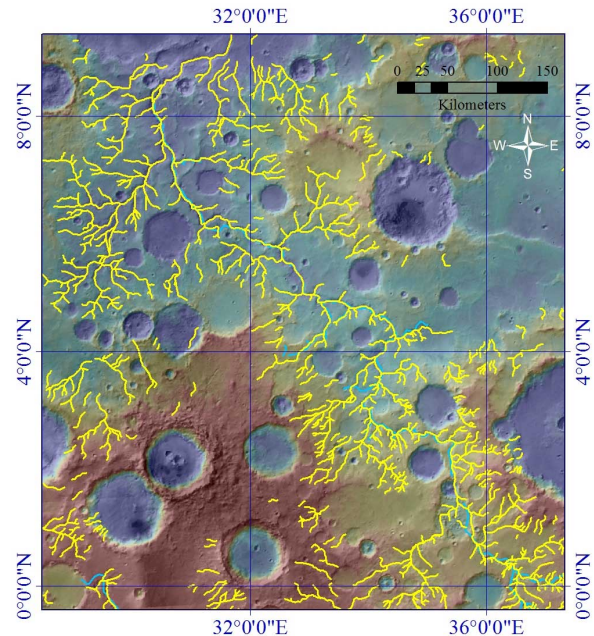


Figure 1. Valley networks (yellow segments) mapped in Arabia Terra using a combination of the MOC wide angle global image mosaic and MOLA elevation data [21]. Blue segments show valley networks mapped earlier using Viking images [37].

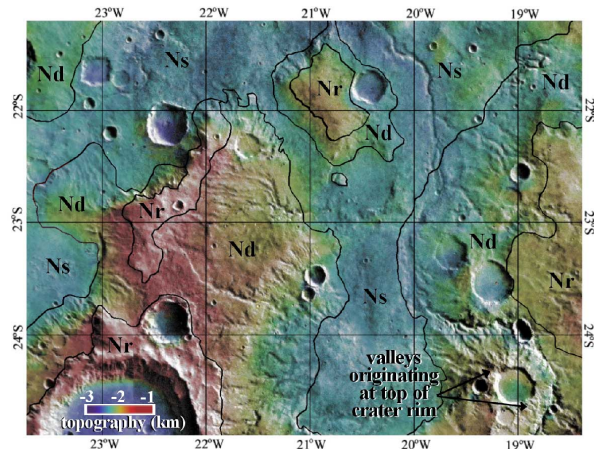


Figure 2. Combined Viking imagery and MOLA elevations in the Margaritifer Sinus region show relationships between undissected Noachian inliers (Nr), portions of the inliers that were dissected by middle to late Noachian valley networks (Nd), and a depositional unit derived from erosion of older Noachian terrain (Ns). The erosional event stripped and/or buried valleys. From [25].

Noachian Climate: Given the difficulty of creating models that produce a sustained warm and wet Noachian period, there are additional possibilities that might explain the formation of valley networks, widespread erosion, and the development of extensive layered deposits, some of which may have an aqueous origin [28]. Water is the most likely agent to produce both valley formation and substantial erosion. Temperatures could have been sub-freezing and precipitation in the form of snowfall, with subsequent basal melting percolating downwards into the ground. This process may operate in the current martian climate [29], but with less vigor.

It is also possible that there were episodic perturbations to the Noachian climate that created, for short periods of geological time, conditions favorable for rainfall or snowfall. Basin-forming impacts may have increased surface and interior temperatures significantly, delivered large quantities of water vapor to the atmosphere, and provided a transient climate favorable for valley formation and erosion [20]. However, valley network formation and widespread erosional events occur to the end of the Noachian (and beyond), past the formation dates of the largest impact basins. This model would have to fashion similar conditions with relatively numerous but less energetic impact events.

Episodic volcanism is another possible mechanism for perturbing the climate, as recognized for Earth [30]. The construction of Tharsis can deliver substantial quantities of water and CO₂ to the atmosphere. A global equivalent layer of 120 m of water and a 1.5 bar CO₂ atmosphere have been estimated [1], and preliminary modeling has explored the climatic implications of Tharsis outgassing [31]. We have little information on the level of episodicity of Tharsis construction. The rate at which volatiles were supplied to the atmosphere versus the rate at which they were removed [e.g., by carbonate deposition (little observed), solar wind stripping, thermal escape, and impact erosion] would dictate the role of Tharsis in perturbing the climate sufficiently to carve valley networks and foster widespread erosion events.

Noachian Evolution: Early Noachian tectonic evolution was dominated by the development of the crustal dichotomy and formation of major impact basins. Subsequently, the construction of Tharsis dominated Noachian volcanic and tectonic processes. The main features of Noachian volatile and climate evolution have been summarized in [32]. Climate was controlled by the volatile history, which involved competition between sources (primordial, comet/asteroid delivery, and volcanism) and sinks, as mentioned above. The magnetic field played a crucial role in protecting the atmosphere from the solar wind loss processes of

pick-up-ion sputtering and hydrodynamic collisions. Thus, understanding the history of the magnetic field [33] is crucial for understanding the climate history.

It is clear that by the end of the Noachian, the bulk of the valley networks had formed and the erosion rate was steeply declining [17]. Isotopic evidence in martian meteorite ALH84001 suggests that the atmosphere was largely unfractionated near the end of the Noachian [34, 35]. The geologic and isotopic information taken together suggests a relatively rapid loss of atmosphere as Mars entered the Hesperian era. Loss of a global magnetic field has been an attractive mechanism, but when the global field declined is a continuing matter of contentious debate.

Figure 3 is a diagram meant to place, in a relative temporal relationship, major events in the Noachian (and later). Most of the entities are discussed in this abstract and/or in [32]. Some of the major basins are shown; noteworthy is the Ares basin, which may have formed while a global field was still active [36], as evidenced by the presence of strong magnetic anomalies within the basin proper. The time span in the early Noachian between the formation of the Ares and Acidalia basins may mark the major decay period of a global field. This is difficult to reconcile with a substantial atmosphere existing until the end of the Noachian unless it was protected by regional remanent magnetic fields [32]. This may provide more weight to the argument that Tharsis, constructed almost exclusively during the Noachian [1], was at least partially responsible for maintaining the atmosphere through the release of large amounts of volatiles.

In summary, on Noachian Mars there was a strong interplay among geodynamic, atmospheric and geologic processes. Tharsis is largely a constructional phenomenon, although its origins can be traced to a warm, buoyant mantle in the western hemisphere. Valley networks and widespread Noachian erosion imply strongly that there were significant precipitation events, frozen and/or liquid, in the Noachian, even if the valleys formed dominantly by groundwater sapping. If temperatures never rose above freezing, there must have been a water supply available to produce sufficient snow to carve the valleys and denude the landscape. Some of this water may have been recirculated in the crust back to the atmosphere. Precipitation may have occurred in short bursts associated with major impact or Tharsis magmatic events. Lack of olivine weathering points to this as well as to generally sub-freezing temperatures. Whatever conditions led to precipitation ceased to exist near the end of the Noachian; leading suspects are the loss of a global magnetic field and the waning of Tharsis magmatism.

- References:** [1]] Phillips R. J. *et al.* (2001) *Science*, 291, 2587. [2] Banerdt W. B. and Golombek M. P. (2000) *LPS XXXI*, Abstract #2038. [3] Anderson R. C. *et al.* (2001) *J. Geophys. Res.*, 106, 20,563. [4] Hartmann W. K. (1973) *Icarus*, 19, 3943. [5] Carr M. H. (1974) *J. Geophys. Res.*, 79, 20,563. [6] Harder H. and Christensen U. (1996) *Nature*, 380, 507. [7] Harder, H. (2000) *Geophys. Res. Lett.*, 27, 301. [8] Solomon S. C. and Head J. W. (1982) *J. Geophys. Res.*, 87, 9755. [9] Phillips R. J. *et al.* (1990) *J. Geophys. Res.*, 90, 5089. [10] Johnson C. L. and Phillips R. J. (2003) *LPS XXXIV*, Abstract # 1360. [11] Dohm J. M. *et al.*, (1997), *LPS XXVIII*, Abstract # 1642. [12] Zhong S. (2002) *J. Geophys. Res.*, 107, doi:10.1029/2001JE001589. [13] Zhong S. and Roberts J. T. (2003), *Earth Planet. Sci. Lett.*, submitted. [14] Mège D. and Masson P. (1996) *Planet. Space Sci.*, 44, 1499. [15] McKenzie D. and Nimmo F. (1999) *Nature*, 397, 231. [16] Johnson C. L. and Phillips R. J. (2003), this conference. [17] Carr M. H. (1996) *Water on Mars*, Oxford Univ. Press, New York. [18] Christensen P. R. *et al.* (2001) *J. Geophys. Res.*, 106, 23,823. [19] Mischna M. A. (2000) *Icarus*, 145, 546. [20] Segura T. L. *et al.* (2002) *Science*, 298, 1977. [21] Hynek B. M. and Phillips R. J. (2003) *Geology*, submitted. [22] Carr M. H. and Chuang F. C. (1997) *J. Geophys. Res.*, 102, 9145. [23] Craddock R. A. and Maxwell T. A. (1993) *J. Geophys. Res.*, 98, 3453. [24] Craddock R. A. and Howard A. D. (2002) *J. Geophys. Res.*, 107, doi:10.1029/2001JE001505, 2002. [25] Hynek B. M. and Phillips R. J. (2001) *Geology*, 29, 407. [26] Carr M. H. and Malin M. C. (2000) *Icarus*, 146, 366. [27] Carr M. H. (2002) *J. Geophys. Res.*, 107, doi:10.1029/2002JE001845. [28] Malin M. C. and Edgett K. S. (2000), *Science*, 290, 1927. [29] Christensen P. R. (2003) *Nature*, 422, 45. [30] Sigurdsson H. (1990) In *Global catastrophes in Earth history*, GSA Special Paper 247, 99. [31] Bullock M. A. *et al.* (2001) *Eos. Trans. AGU*, 82 (47), Fall Meet. Suppl., Abs., F708. [32] Jakosky B. M. and Phillips R. J. (2001) *Nature*, 412, 237. [33] Stevenson, D. J. (2001) *Nature*, 412, 214. [34] Marti K. and Mathew K. J. (2000), *Geophys. Res. Lett.*, 27, 1463. [35] Mathew K. J. and Marti K. (2001) *J. Geophys. Res.*, 106, 1401. [36] Frey H. V. (2003) *LPS XXXIV*, Abstract # 1838. [37] Carr M. H. (1995) *J. Geophys. Res.*, 100, 7479.

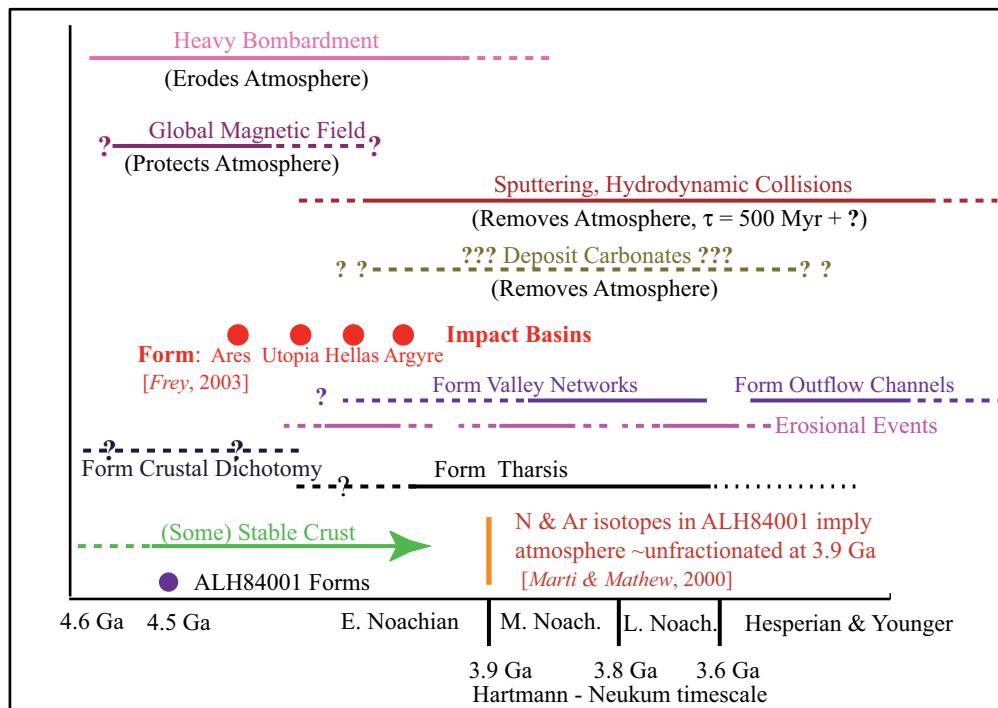


Figure 3. Major events and their interrelationships in the Noachian (and later). Diagram is intended as a thought tool and is thus subject to constant revision. The time axis is definitely not linear. τ is the characteristic timescale for atmospheric removal by solar wind processes.

Polygonal landforms at the South Pole and implications for exposed water ice. S. Piqueux¹, S. Byrne¹, M.I. Richardson¹, ¹Division of Geological and Planetary Sciences, California Institute of Technology, Mail-stop 150-21, 1200 East California Blvd., Pasadena, CA 91125, USA. sylvain.piqueux@free.fr, shane@gps.caltech.edu, mir@gps.caltech.edu

Introduction: Polygonal terrain (see Fig. 1) is a reliable indication of subsurface water ice [1,2]. Following the discovery of exposed water ice on the south polar layered deposits [3] we searched for and mapped occurrences of polygonal terrain. Occurrences of polygons were found in regions interpreted to have exposed water ice at the surface.

Mapping: We report on the extension of this mapping to cover the rest of the south polar region. We discuss the possibility of using the distribution of polygonal landforms as a prediction of where exposed water ice will be expected to be found in the upcoming southern summer. This years observations will be much more complete than last years.

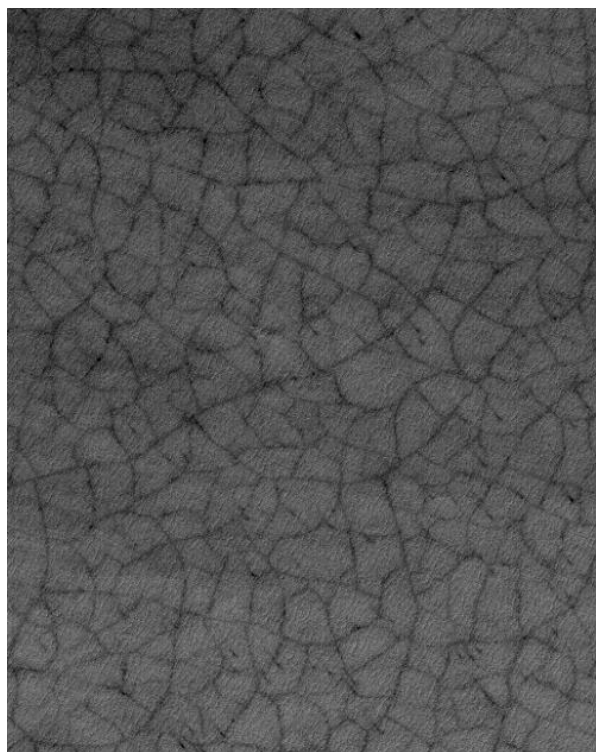


Figure 1. Subframe of M09/05958 showing typical polygons. Frame is 3km across.

Roughness: Polygonal areas are well correlated with smooth areas. We will report on correlations between roughness (measured by rms slope) and concentration of polygonal features.

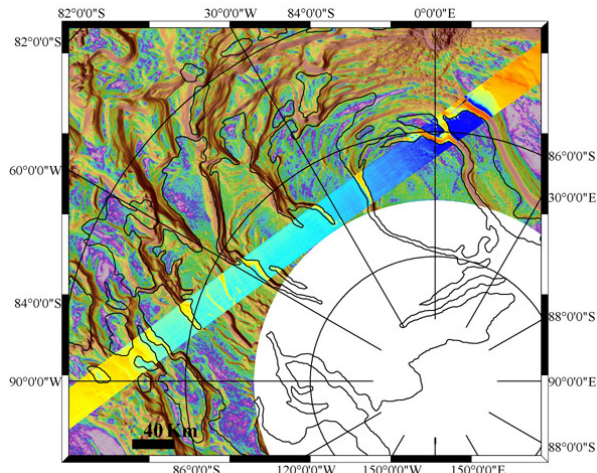


Figure 2. Background is roughness map (rms slope on 1km baselines) where purple is smooth and brown rough. Overlain is THEMIS IR frame I00910002 which was used to demonstrate exposed water ice at roughly 10° E.

The exposed water ice unit [3] spans a larger roughness range. The connections between exposed water ice, polygonal landforms and surface roughness will be discussed in more detail.

References: [1] Mellon, M.T. (1997) *JGR*, 102, 25617-25628. [2] Plug, L.J. and B.T. Werner (2002) *Nature*, 417, 929-933. [3] Titus, T.N., et al. (2003) *Science*, 299, 1048-1051.

Automated Feature Extraction and Hydrocode Modeling of Impact Related Structures on Mars: Preliminary Report. C. S. Plesko¹, E. Asphaug¹, S. P. Brumby², and G. R. Gisler², ¹University of California, Santa Cruz, Earth Sciences Dept. cplesko@es.ucsc.edu, ²Los Alamos National Laboratory.

Introduction: We have begun a systematic, combined modeling and observation effort to correlate Martian impact structures – craters and their regional aftermaths – to the impactors, impact processes and target geologies responsible. When the cratering process is modeled in 3D, so that azimuthal heterogeneity is accommodated, one can seek best-fits to regional or even global distributions of radial fractures, crater rays and secondary streamers.

We are pursuing this cratering work on two fronts, (1) using automated feature extraction techniques to identify the extensive impact-related features on Mars, and (2) leveraging these impact features through impact modeling (using the 3D SPH and SAGE hydrocodes) to tell us about the specific target response to impact, and hence Martian geology.

We are motivated to do this because the Mars data set is now rich with well-characterized impact features, many of them recent and detailed, and because azimuthal asymmetry in cratering has never been adequately modeled in this context. The asymmetry of crater ejecta (rays and secondary streamers) is probably related to the asymmetry of ejecta from catastrophic disruption events in asteroid disruption¹, a subject which also suggests that the delivery of meteorites from the surface of Mars may be easier to understand in 3D than in 2D.

Impact Structures: Keys to the subsurface geology of every cratered body can be found in the study of its impact structures. But interpretations of the cratering process on planets are diverse, and Mars is no exception. For example, there exists no consensus among crater geologists and modelers on the process of crater rebound. Despite decades of intensive research in this area, we must confess to a broad ignorance regarding how large craters form. The hypothesis of panspermia² – that planets can swap rocks via impact ejection and perhaps exchange the seeds of life – is supported by the SNC meteorites, but the process by which these rocks were ejected from Mars remains controversial^{3,4}. Vickery⁵ first attempted to use crater secondaries (around Copernicus on the Moon, Lyot on Mars, and others) as “witness plates” of the size-velocity distribution of ejecta from a crater, since secondary distance from primary easily relates (on an airless body) to ejection velocity, and secondary diameter relates to ejecta fragment diameter. Asphaug¹ made use of this work to calibrate impact hydrocodes in a planetary setting, and used it to explain ejection of V-

type asteroids from asteroid 4 Vesta. Vickery⁵ together with her undergraduate assistants lost the secondary craters in the background population beyond a few crater radii, so that the fast “tail” of ejecta fragments (those most relevant to panspermia) remained uncharacterized. Bierhaus et al.⁶ made use of the extraordinarily fresh ~26 km diameter impact structure Pwyll on Europa to characterize ejection patterns at global distances. Pwyll’s secondaries were used by Moore, Asphaug, and others⁷ to explore whether the crater formed in an ice shell over liquid water, or in solid ice, the distal secondaries and rays from Pwyll have yet to be fully exploited to constrain Europa’s geology.

Mars, especially in the post-THEMIS era, opens up a treasure trove for planetary impact modelers. Notably, impact craters have been discovered on Mars to be accompanied by associated structures that extend for many hundreds of kilometers, including detailed ray patterns and secondary streamers. The most stunning example is the fresh crater of the Cerberus plains presented by McEwen et al. (2003)⁸. We are using automated feature detection software to map the extent and distribution of such structures by keying to the desired signature (e.g. ray patterns) in the multispectral THEMIS imagery.

Automated Feature Detection:

GENIE. Los Alamos National Laboratory’s GENIE system⁹ is an innovative machine learning software package using techniques from the fields of genetic algorithms^{10,11} and genetic programming¹² to construct custom feature extraction algorithms for remotely sensed imagery^{13,14}. It was developed to allow rapid development of image analysis software tools for multispectral and hyperspectral imagery in the context of Earth remote sensing¹⁵. GENIE is particularly well suited to exploratory analysis of multi-wavelength imagery for which spatial/textural as well as spectral signatures can help identify features of interest, as well as analysis of imagery for which there do not yet exist the detailed atmospheric models needed to turn at-sensor radiances into at-surface material properties (reflectances and emissivities). This is precisely the case facing scientists carrying out initial analysis of high resolution THEMIS data.

Both the structure of the feature extraction algorithm, and the parameters of the individual image processing steps, are learned by the system. The format of an algorithm evolved by GENIE is human-readable code than can be analyzed to understand the

physical signatures of the feature of interest. The evolved algorithms combine spatial and spectral processing, and the system was designed to enable exploration of spatio-spectral image processing of novel datasets. This system has been shown to be effective in detecting complex spatio-spectral terrain features in multispectral and hyperspectral imagery, and has been successfully applied to a number of real-world problems, including analysis and mapping of ash/debris from the September 11 attack on New York City and analysis and mapping of the burn scar following the Los Alamos Cerro Grande wildfire¹⁶.

GENIE begins by randomly generating a population of candidate image-processing algorithms from a collection of spectral and spatial/textural image processing operators, including local neighborhood statistics, texture measures, spectral band-math operations (e.g. ratios of bands), and gray-scale morphological filters with various shapes of structuring elements. Each candidate algorithm consists of a number of these image-processing operators, which together generate a vector of processed images in an intermediate, non-linear feature space. These are combined using a Fisher linear discriminant to produce a single gray-scale result image in which bright pixels indicate the presence of the feature of interest. This gray-scale result is converted to a Boolean classification using an optimal threshold¹⁷. The parameters of the Fisher discriminant and threshold are based on training data provided by the human user via GENIE's graphical interface. Our fitness metric for evaluating candidate image-processing algorithms measures the total error rate (false positives and false negatives) calculated from the training data. After a fitness value has been assigned to every candidate algorithm less fit members of the population are discarded. A new population is generated by allowing the most fit members of the old population to reproduce with modification via the evolutionary operators of mutation and crossover. To ensure a monotonic increase in fitness the most fit individual in the current population is kept without modification (principle of elitism). This process of fitness evaluation and reproduction with modification is iterated until the population converges, or some desired level of classification performance is attained, or some user-specified limit on computational effort is reached (e.g., a limit on the number of candidate algorithms evaluated). This Boolean threshold on the best image processing algorithm returned by GENIE may be adjusted by the user to re-adjust the emphasis of detection rate (true positives) over false alarms and missed detections. There is often more than one solution to a particular feature extraction question, in which case the results of several different algorithms

trained on the same training data may be combined to increase detection accuracy and lower false alarm rates¹⁸.

Past Efforts. Past Mars-related GENIE efforts have focused on crater extraction in panchromatic Mars Orbiter Camera imagery. GENIE was able to generate algorithms that detect craters in images it was not trained on with 94% detection and 2% false alarm rates compared to a manual crater survey¹⁹.

Applications to Impact Modeling. GENIE is an extremely powerful tool for extracting features from large numbers of images, and especially for multispectral data, which it can process more readily than a human analyst. We will use GENIE to explore relationships between impact related features which are obvious to a human analyst, and use them to search for less obvious features, such as crater ray material farther downrange of the impact than is immediately obvious to the analyst.

Hydrocode Modeling: GENIE provides the reduced data set to be reproduced with our impact models. We are using Smooth Particle Hydrodynamics (SPH) and the adaptive grid Eulerian hydrocode known as SAGE, both in 3D, to model the formation of the best-preserved crater structures on Mars, the goal being to match not only crater size and shape but also regional aftermath such as secondary crater fields, azimuthal asymmetries, and ejecta rays. Beginning with simple equations of state (e.g. basalt) and moving to sophisticated equations of state for candidate Martian geology (for example saturated versus dry alluvium over basalt) we shall establish initial conditions (target geologies) to be tested for each GENIE-derived data set.

SAGE and SPH: The SAGE code from Los Alamos National Laboratory and Science Applications International Corporation is a compressible Eulerian hydrodynamics code using continuous adaptive mesh refinement (AMR) for following discontinuities with a fine grid while treating the bulk of the simulation more coarsely. In previous work²⁰ we have used tabular equations of state for the atmosphere, water, oceanic crust, and mantle of Earth. We are porting to SAGE the revised ANEOS parameters as well as the sophisticated explicit-fracture treatment developed within the context of Smooth Particle Hydrodynamics (SPH)²¹ for high strain rate fragmentation in planetary impacts. The two codes are based on very distinct numerical techniques (Eulerian AMR vs. gridless Lagrangian), and are therefore of complementary utility, with SAGE being useful for studying atmospheric interaction and SPH being better suited – at present, at least – for studying solid rock fragmentation effects.

Results: The first task is to use GENIE to extract feature signatures of impact, correlated to particular craters on Mars. We shall present our progress in this area, the fundamental goal being a basic set of well-characterized impact outcomes to be modeled with the hydrocodes. By treating each impact structure as a detailed aftermath – not just a crater diameter, for instance – we open up a new, careful, and detailed study of the Martian lithosphere and atmosphere.

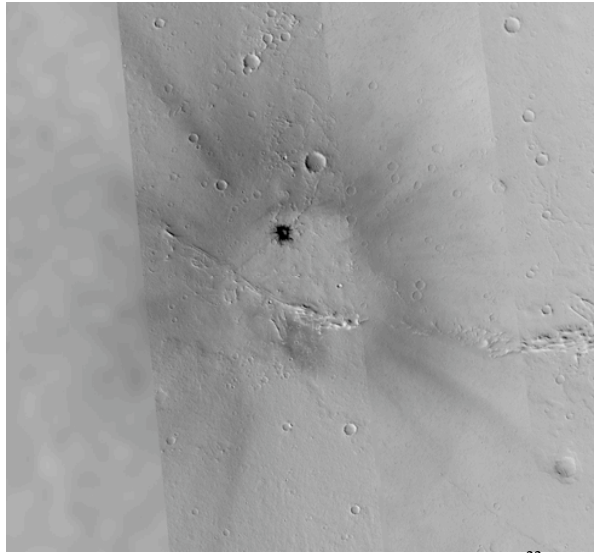


Figure 1. From MGS MOC Release No. MOC2-301.²² A small, unnamed crater (~130 m diameter) is surrounded by a wealth of geophysical detail which can be exploited by the SAGE 3D hydrocode. It is clearly an oblique impact with an airburst followed by core penetration of the surface – perhaps a small comet with a rocky core? Both the structure of the impactor and the response of the Martian atmosphere can be modeled with SAGE's AMR capability. GENIE will search for similar levels of detail, generally hidden in visible imagery, in the THEMIS data sets, correlated to given impact craters. The goal is to produce several complete data sets, for varying sizes of craters, consisting of the crater itself, and the distribution of rays and secondaries.

References: [1] Asphaug, E., (1997) *Meteor. & P. Sci.*, **32**: A9. [2] Melosh, H. J., (1984) *LPSC* **16**:550-551. [3] Head, J. *et al.*, (2002) *Science* **298**:1752-56. [4] Artemieva, N. A., Ivanov, B. A., (2002) *LPSC* **33**:1113. [5] Vickery, A. M., (1993) *Icarus* **105**:441. [6] Bierhaus, E. B. *et al.*, (2001) *Icarus*, **153**:2, 264-276. [7] Moore, J.M. *et al.*, (1998) *Icarus* **135**:1, pp. 127-45. [8] McEwen, A. *et al.*, *LPSC* **34**:2040. [9] Brumby, S.P. *et al.*, (1999) *Proc. SPIE*, **3812**, 24-31, (see <http://www.daps.lanl.gov/genie>). [10] Holland, J.H. (1975) *Adaptation in Natural and Artificial Systems*, U. Mich. [11] Fogel, L. *et al.*, (1966) *Artificial Intelligence through Simulated Evolution*, Wiley. [12] Koza, J.R., (1992) *Genetic Programming: On the Programming of Computers by Natural Selection*, MIT.

[13] Theiler, J. *et al.*, (1999) *Proc. SPIE*, **3753**:416-425. [14] Perkins, S. *et al.*, (2000) *Proc. SPIE*, **4120**:52-62. [15] Harvey, N.R. *et al.*, (2000) *Proc. SPIE*, **4132**:72-82. [16] Brumby, S. P., *et al.*, (2001) *Proc. SPIE*, **4381**:236-245. [17] For example, see Bishop, C.M., (1995) *Neural Networks for Pattern Recognition*, Oxford Univ., 105 –112. [18] Duda, R.O. *et al.*, (2001) *Pattern Classification*, 2nd ed., Wiley-Interscience. [19] Plesko, C.S. *et al.*, (2003) *LPSC* **34**:1758. [20] Gisler, G. R. *et al.*, (2002) *AAS* **200**:59.03. [21] Benz, W., and E. Asphaug, (1995) *Comput. Phys. Commun.* **87**:253-265. [22] Malin, M.C. *et al.*, (2003) <http://photojournal.jpl.nasa.gov/>, Catalog number E0501904.

THE COMPOSITION OF MARTIAN LOW ALBEDO REGIONS REVISITED. F. Poulet, S. Erard, IAS, Université Paris-Sud, 91405 ORSAY Cedex, France (francois.poulet@ias.u-psud.fr), N. Mangold, Orsayterre, Université Paris-Sud et CNRS, 91405, Orsay Cedex, France.

Introduction: Low albedo regions on Mars are often interpreted as outcrops of volcanic rocks. Mineral models of the thermal emission spectra obtained by TES indicate that the martian dark regions are characterized by basaltic surface material: large fraction of feldspar and one high-calcium pyroxene [1]. The data from the IR spectrometer ISM onboard Phobos-2 show that the composition of these layers is rich in pyroxenes and contains a significant signature of hydration [2]. A systematic comparison of TES and ISM data suggests that variations in the vis-NIR observations could be controlled by dust or other thermally neutral materials [3]. The purpose of this work is to revisit the surface composition of dark regions by modeling ISM spectra representative of dark regions with a radiative transfer theory and taking in account new high resolution images which give a new view of the surface texture of these regions. Syrtis Major and dark spots inside chasmata of Valles Marineris are of particular interest. Even if it is important to remember that the different observational techniques (visible, NIR and thermal) are sensitive to different characteristics of the martian surface, the understanding of discrepancies of the compositional analysis from different measurements and the nature of low albedo layers is essential 1- to understand their erosional history, and 2- to interpret the IR data of future spectrometers like OMEGA and PFS onboard Mars Express.

Geomorphic analysis: Low albedo regions were usually interpreted as bedrock despite the fact that fields of dark dunes have been observed at Viking images scale. The study of MOC high resolution images and THEMIS IR data show that the proportion of bedrock in these low albedo regions is small. First, in Valles Marineris, many dark areas correspond to dark sand sheets [4]. These areas are typically smooth and devoid of craters at MOC scale (Fig. 1). They have the thermal response of sandy materials on THEMIS IR images. On the other hand, MOC images of Syrtis Major shows a surface texture different of volcanic bedrock (Fig. 2). No lava flows are observed and large craters are partially filled by smooth material. Furthermore, there are few small craters showing the occurrence of a process of resurfacing in recent times, less than ten million years ago. Only progressive dust deposition and eolian filling can explain such youthful smooth mantling, similar to that observed in regions like Arabia Terra for bright dust. Such filling is observed in most locations West of the two pateras, so in the very low albedo region. THEMIS data confirm that material at surface

has mainly the thermal response of silt-sand size grains but not of bedrock, except on the pateras. Thus the low albedo regions, in which we can look for the composition using ISM data, are correlated with dark sand dunes, sand sheets and eolian dust mantling but not obviously bedrock. Dust is usually bright material but dark silt, maybe in a bit coarser particles compared to bright dust, has been proposed to exist in the past from both spectroscopic or geomorphic analysis [5,6]. Its existence is still controversial and the composition of such dark silt able to be transported in suspension in the atmosphere is questionable.

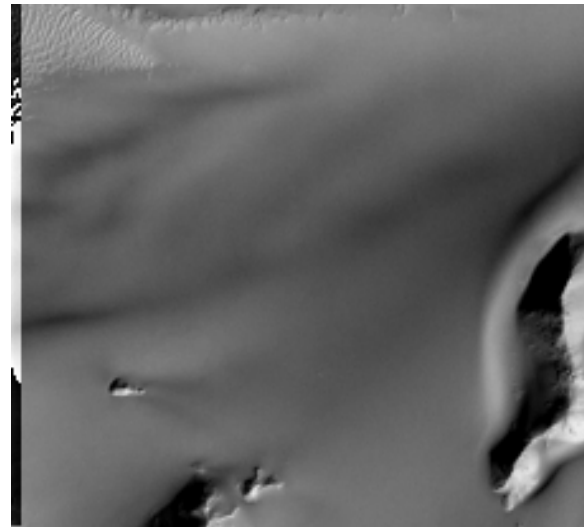


Fig. 1: MOC images (width: 2 km) of sand sheet inside dark region on the floor of West Ganges Chasma. Note smooth wave typical of sandy material.

Spectral data: The data used are from the PDS archive on www.ias.fr/cdp/Base/ISM/INDEX/HTM. Two ISM windows (Aurorae and Syrtis-Isidis) were used in this study. The basic approach is to extract the spectra with albedo (with aerosols scattering and photometric corrections) lower than 15%. This selection (about 700 spectra for each window) should cover most of the terrains studied previously with the MGM method [2]. The spectra are characterized by 1- and 2-micron absorptions and gray/slightly red slope between 0.8 and 2.5 microns.

Choice of the scattering model: We choose to use the Shkuratov radiative transfer theory for fitting the spectra [7]. This geometrical optics model based on the slab approximation for calculating the albedo of a particle has been compared to other scattering models [8] and

tested with laboratory mineral mixtures [9].

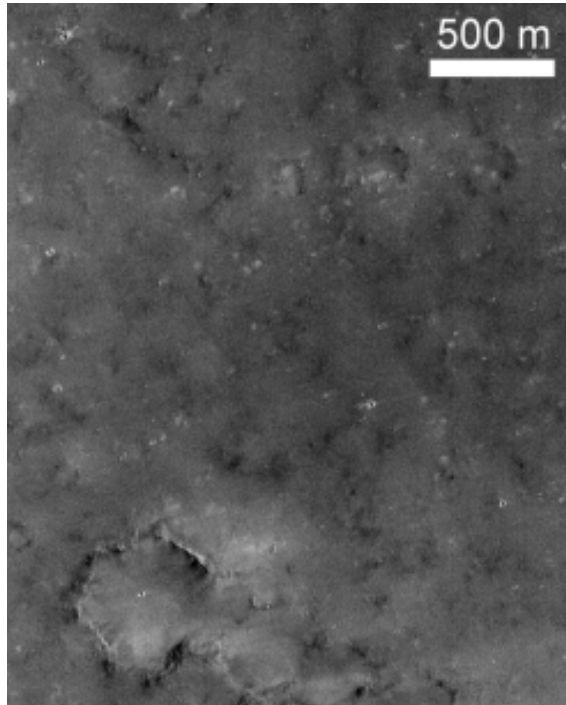


Fig. 2: MOC image of West Syrtis Major. Smooth texture with few craters and no lava flows visible.

Choice of the optical constants and end-members:

We select the surface composition of each spectrum by trying to satisfy the following spectral characteristics: low albedo, shape and depth of 1- and 2-micron absorptions and spectral slope. Low- and high-calcium pyroxenes were obviously included in the scattering calculations. Spectrally featureless low albedo component in near-infrared to lower the average spectral reflectance is also required. Oxides such as magnetite display this neutral opaque behavior. Hematite (ferric oxide) was also considered because of its low albedo and its 0.85 micron absorption. Other minerals such as common amphiboles, obsidians and phyllosilicates were included in some scattering calculations. However, the presence of such minerals is unlikely because they present prominent OH- and H₂O- features with only a very few amount (5%) as shown in Fig. 3. Other common minerals with weaker absorptions such as feldspar and olivine were considered. The optical constants of endmembers were calculated from endmember reflectance spectra extracted of the RELAB library by following the procedure described in [9].

Choice of the type of surface and results: Three types of surface are investigated: dust (mixture of particles of size \ll wavelength), sand (intimate mixture of particles of size \gg wavelength), dust/sand mixture.

The optimization of abundances and grain sizes of endmembers is done by a downhill simplex technique.

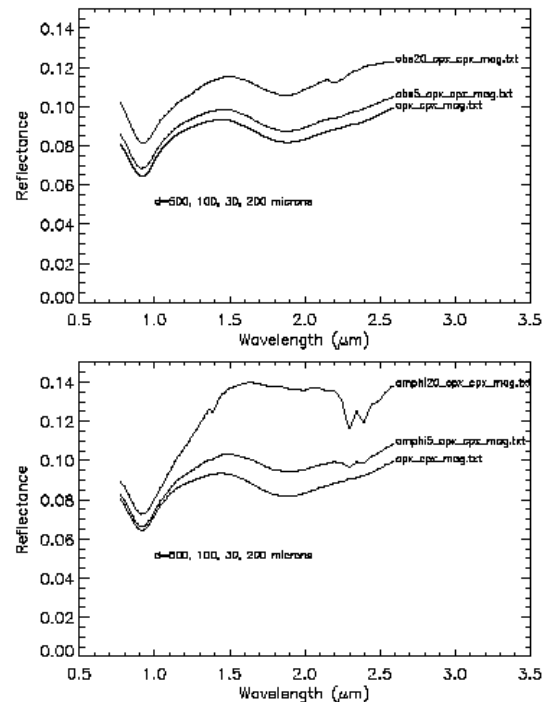
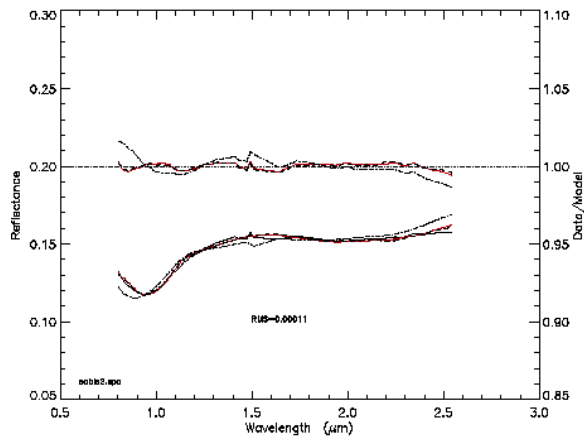


Fig. 3: (top): Three synthetic spectra of an intimate mixture of one obsidian, two pyroxenes and a dark component (here magnetite). The size of coarse particles for each components indicated. The concentration of obsidian is 20%, 5% and 0%. (bottom): Same except for obsidian replaced by amphibole.

The dust mixture fails to reproduce the spectra (Fig. 4). The spectra are well reproduced by a mixture of coarse particles pyroxenes / hematite / magnetite / olivine / feldspar. However, the very large proportion ($> 50\%$) of hematite and magnetite coarse particles (size of several hundred microns) necessary for achieving the low albedo would have been detected by TES observations [1]. The best fits of the 0.8-2.5 micron spectra are obtained with a mixture of five components: a four component intimate mixture of two pyroxenes, olivine, and hematite mixed with a large proportion of dusty grains of hematite and magnetite (55%). We outline that both low- and high-calcium pyroxenes are required in agreement with [2]. The presence of large quantity of feldspar is very unlikely because this mineral is quite bright in the near-infrared. By contrast, the calculated large fraction of dust is in favor of a surface dust-coated rather than rock outcrops. Fig. 5 shows the distribution of the mixing ratios of the five components for low albedo regions located in the eastern part of Valles Marineris. The low dispersions suggest that



most units are similar in composition, hidden by homogenized surface materials, or some combination of Fig. 4: A representative low albedo spectrum (thick line) and three synthetic spectra made of seven-component dust (dotted-dashed line), seven-component intimate mixture (dashed line), and four-component mixture mixed with dust (thick red line). The data/model ratio allows a rapid qualitative assessment of the accuracy of the fits. The value of the RMS for the sand/dust mixture is indicated.

both. Even if further modeling need to be done, no significant difference of composition between the two studied ISM windows (Aurorae and Syrtis) were found so far. Also, the disconnect between ISM and TES observation modeling may result from the fact that NIR data are much more sensitive to thin coatings than thermal IR data, so that TES data may not detect large amounts of oxide mineral dust.

References: [1] Hamilton et al. (2001) *JGR* 106, 14733–14746. [2] Mustard et al. (1997) *JGR* 102, 25605–25615. [3] Cooper C.D. and Mustard J.F. (2002), *AGU* P51C-07. [4] Mangold et al. (2003) *EGS/AGU* abstract. [5] e.g. Dollfus et Deschamps, (1993) *JGR*, 98, 3413-3429. [6] Edgett and Malin (2000) *JGR*, 105, 1623-1650. [7] Shkuratov et al. (1999) *Icarus* 137, 235–246. [8] Poulet F. et al. (2002) *Icarus* 160, 313–324. [9] Poulet et al. (2003) *LPSC* XXXIV, abstract.

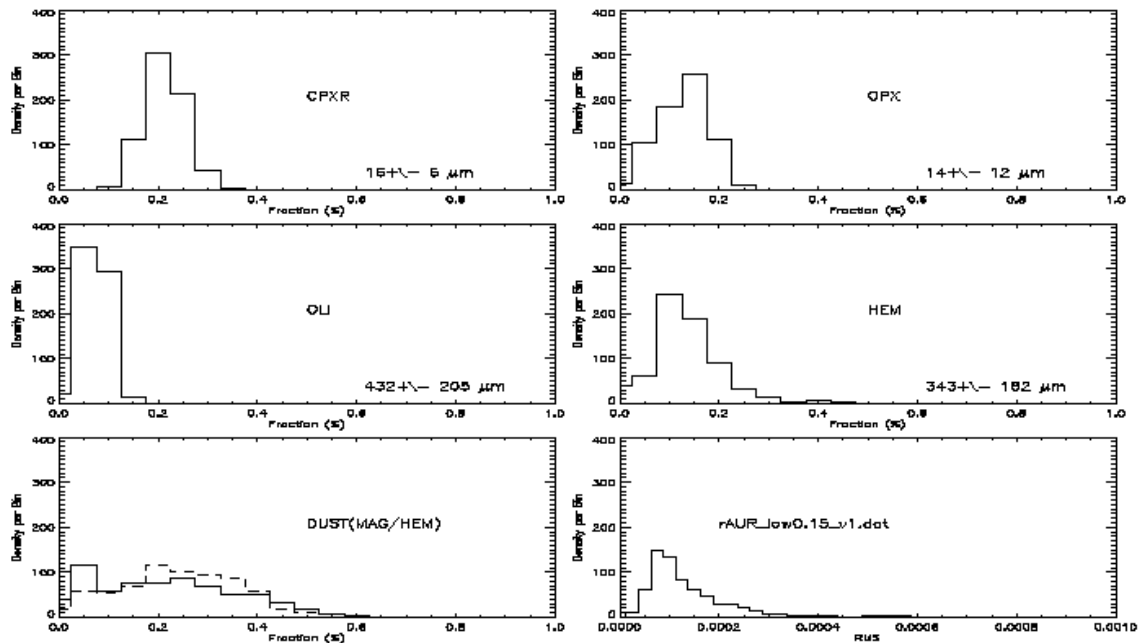


Figure 5: Histograms of calculated mixing ratios of each component and RMS of fits for the low albedo spectra extracted from the ISM Aurorae window. A sand+dust mixture is considered. The mean value of coarse grain size for each component is indicated.

MID-LATITUDE COMPOSITION OF MARS FROM THERMAL AND EPITHERMAL NEUTRONS.

T.H. Prettyman,¹ W.C. Feldman,¹ R.C. Elphic,¹ W.V. Boynton,² D.L. Bish,¹ D.T. Vaniman,¹ H.O. Funsten,¹ D.J. Lawrence,¹ S. Maurice,³ G.W. McKinney,¹ K.R. Moore,¹ and R.L. Tokar¹ ¹Los Alamos National Laboratory, Los Alamos, New Mexico. ²Lunar and Planetary Laboratory, University of Arizona, Tucson. ³Observatoire, Midi-Pyrenees (Toulouse, France).

Introduction: Epithermal neutron data acquired by Mars Odyssey have been analyzed to determine global maps of water-equivalent hydrogen abundance [1]. By assuming that hydrogen was distributed uniformly with depth within the surface, a map of minimum water abundance was obtained. The addition of thermal neutrons to this analysis could provide information needed to determine water stratigraphy. For example, thermal and epithermal neutrons have been used together to determine the depth and abundance of water-equivalent hydrogen of a buried layer in the south polar region [2,3].

Because the emission of thermal neutrons from the Martian surface is sensitive to absorption by elements other than hydrogen, analysis of stratigraphy requires that the abundance of these elements be known. For example, recently published studies of the south polar region [2,3] assumed that the Mars Pathfinder mean soil composition is representative of the regional soil composition. This assumption is partially motivated by the fact that Mars appears to have a well-mixed global dust cover and that the Pathfinder soil composition is representative of the mean composition of the Martian surface [4].

In this study, we have analyzed thermal and epithermal neutron data measured by the neutron spectrometer subsystem of the gamma ray spectrometer to determine the spatial distribution of the composition of elements other than hydrogen. We have restricted our analysis to mid-latitude regions for which we have corrected the neutron counting data for variations in atmospheric thickness.

Composition or Stratigraphy? The emission of epithermal neutrons from Mars is sensitive to hydrogen abundance and stratigraphy to within about a meter of the surface. Thermal neutrons are also sensitive to hydrogen abundance and stratigraphy; however, because the cross section for thermal neutron capture is large at thermal energies, they are also sensitive to the composition of elements such as Fe and Cl, as well as rare earth elements, Gd and Sm, which have large absorption cross sections. Consequently, thermal and epithermal neutrons cannot be used to independently determine water abundance and stratigraphy when the composition of major elements other than hydrogen is unknown.

To illustrate this point and to gain some insight into whether composition varies in the mid-latitudes, we

analyzed measured neutron count rates for selected regions in Tharsis. Epithermal and thermal neutron count rate maps are shown in Figs. 1 and 2, respectively, for the western hemisphere mid-latitudes ($\pm 60^\circ$ latitude and -180° to 0° east longitude). These 2° quasi-equal-area maps were constructed using data acquired from the beginning of mapping in late February 2002 ($L_S=346^\circ$) through January 2003 ($L_S=131^\circ$). The maps have been corrected for variations in atmospheric mass to enable comparison to neutron count rates calculated for an atmospheric mass of 16 g/cm^2 [5]. The thermal and epithermal count rate model that we used for this study takes into account the ballistic trajectories of the neutrons and their half life, the velocity and orbit of the spacecraft, and the response function of the neutron spectrometer. The model was calibrated using data acquired near the north pole when the seasonal CO_2 frost was thickest [1].

Three regions of interest are shown on the thermal neutron map: Region A contains the Tharsis volcanic shields, including Olympus Mons; Region B contains Solis Planum; and Region C contains the highlands surrounding Solis Planum and extends into Valles Marineris. A scatter plot of thermal and epithermal count rates measured within these regions is shown in Fig. 3. Also shown in Fig. 3 are calculated count rates for three different surface materials mixed with variable amounts of water-equivalent hydrogen. The materials are: Mars Pathfinder mean soil (labeled "Soil" in Fig. 3) and soil-free rock (labeled "Andesite" in Fig. 3), and shergotty (labeled "Basalt" in Fig. 3) [4,6].

The red curves in Fig. 3 show the variation of count rate with water abundance for each of the three materials for the case in which the distribution of water is uniform with depth. Count rates are shown for water abundances ranging from 0.5% to 100% for the soil composition and from 0.5% to 10% for basalt and andesite. The epithermal neutron count rate decreases with increasing water abundance and is relatively insensitive to other changes in composition. The thermal neutron count rate, as indicated by the red curves is strongly sensitive to material type (soil, andesite, or basalt) due to variations in major absorbers.

The macroscopic absorption cross section for thermal neutrons was determined to be 11.6 capture units ($1 \text{ c.u.} = 10^{-3} \text{ cm}^2/\text{g}$) for the soil, 9.1 c.u. for andesite, and 7.9 c.u. for the basalt. Changes in Cl and Fe abundance between the materials account primarily for the differences in the absorption cross section and the

simulated count rates. However, Cl, which has an absorption cross section that is 13 times that of Fe, dominates the variation in the macroscopic absorption cross section. We used a Cl composition of 0.55% by weight for the soil, 0.32% for the andesite, and 0.01% for the basalt.

The red curves in Fig. 3 give an upper bound on thermal neutron count rates for a given material type (soil, andesite, or basalt). It is possible to achieve lower count rates by varying the stratigraphy of hydrogen. We have modeled cases in which a water-rich layer is buried beneath relatively dry material. Such cases are indicated in Fig. 3 for the soil composition by dashed lines and symbols. One set of cases, corresponding to 100% water buried beneath different amounts of soil containing 1% water, is labeled with the depth of the buried water-rich layer in g/cm^2 . Note that in the limit, as depth of the water rich layer increases, the count rate approaches that of the dry upper layer.

The measured thermal count rates for the volcanic shield region (Region A, shown as red symbols in Fig. 3) exceed the maximum count rate that can be achieved for Mars Pathfinder soil, as indicated by the red curve labeled "Soil." The count rates are more consistent with the basalt composition. The thermal neutron count rates in Solis Planum (Region B, shown as green symbols in Fig. 3) are also more consistent with basalt than with soil. The thermal neutron count rates for the highlands surrounding Solis Planum (Region C, shown as yellow symbols in Fig. 3) are lower but still exceed the maximum count rate expected for Pathfinder soil. Thermal neutron count rates for the western hemisphere mid-latitudes (shown as blue symbols in Fig. 3) extend below the maximum count rate for Pathfinder soil. Consequently, some regions with composition consistent with the soil exist in the western hemisphere between latitudes $\pm 40^\circ$. However, the regions examined in Tharsis are not consistent with this composition, probably due to relatively low Cl abundance associated with volcanic materials. Note that small variations in Cl abundance can significantly affect the thermal neutron output because the cross section for Cl is large. It is not possible to determine from thermal and epithermal neutrons alone whether observed differences in thermal neutron count rate are due to changes in hydrogen stratigraphy or changes in the abundance of thermal neutron absorbers.

Maps of Neutron Cross Sections: Feldman et al. [7] developed and demonstrated methods to determine bulk neutron transport properties of planetary surfaces from orbital thermal and epithermal counting data. Using these methods, we have developed maps of neutron scattering and absorption cross sections for

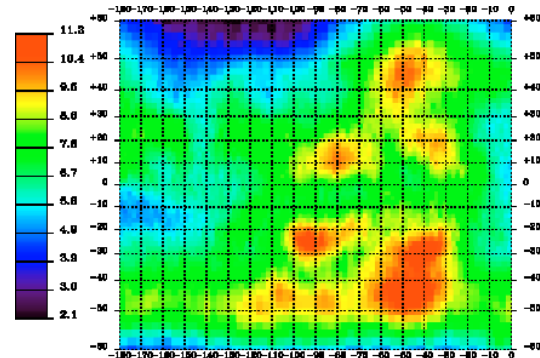


Fig. 1. Map of epithermal neutron count rates (counts/s) in the western hemisphere mid-latitudes ($\pm 60^\circ$ latitude; -180° to 0° east longitude).

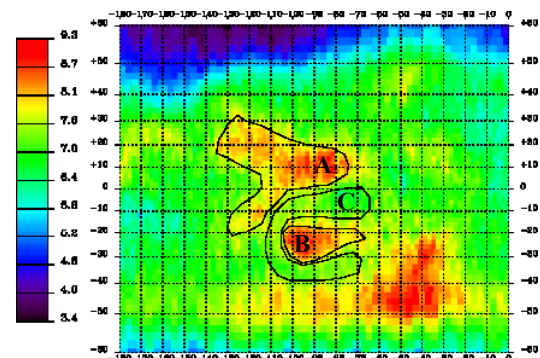


Fig. 2. Map of thermal neutron count rates (counts/s) in the western hemisphere mid-latitudes ($\pm 60^\circ$ latitude; -180° to 0° east longitude). Some regions of interest are shown.

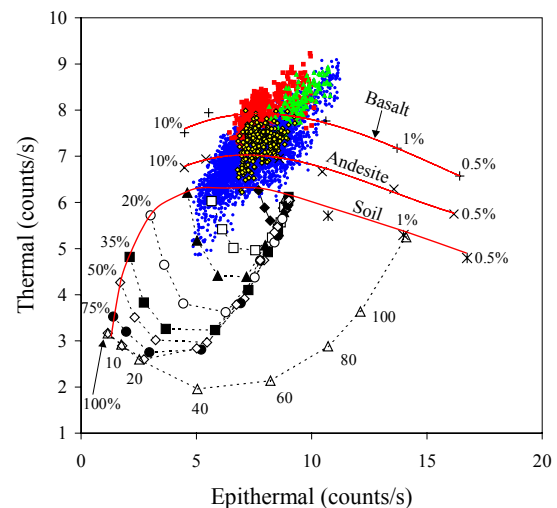


Fig. 3. Simulated and measured thermal neutron count rates are shown. The measured count rates correspond the regions delineated in Fig. 2. Counting data from Region A is shown as red symbols; data from Region B is shown as green symbols; data from Region C is shown as yellow symbols; and data from the western hemisphere between $\pm 40^\circ$ latitude is shown as blue symbols. A description of the simulated count rates is given in the text.

the Martian mid-latitudes. The analysis assumes that there is no variation in composition (hydrogen or otherwise) with depth. Epithermal neutrons are used to determine $\xi\Sigma_s$, the product of the mean fractional energy loss per elastic collision (ξ) and the macroscopic scattering cross section (Σ_s). The ratio of epithermal to thermal neutrons is used to determine $\Delta = \Sigma_a / \xi\Sigma_s$, where Σ_a is the macroscopic absorption cross section for thermal neutrons.

In order to determine the relationship between the measured count rates and the neutron transport parameters, we simulated thermal and epithermal count rates for 60 different compositions, including soil, basalt and andesite with variable amounts of hydrogen and Cl. The materials were selected to span the count rates observed by the Mars Odyssey neutron spectrometer at mid-latitudes. For each composition, we calculated the transport parameters Σ_a , ξ , Σ_s , $\xi\Sigma_s$, and Δ .

Using data from all 60 simulated compositions, we found the following relationship between $\xi\Sigma_s$ and the epithermal neutron count rate:

$$\xi\Sigma_s = 1.5966C_{\text{epi}}^{-1.6091}. \quad (1)$$

The correlation coefficient of the regression was found to be $R^2=0.9988$. We found the following relationship between Δ and the ratio of the epithermal to thermal count rate:

$$\Delta = 0.2146(C_{\text{epi}}/C_{\text{therm}}) - 0.0753, \quad (2)$$

The correlation coefficient for the regression was found to be $R^2=0.9987$. Using Eqs. 1 and 2, we calculated mid-latitude maps of $\xi\Sigma_s$ and Δ , which are shown in Figs. 4 and 5, respectively. A map of Σ_a obtained by multiplying $\xi\Sigma_s$ by Δ is shown in Fig. 6.

Note that the map of $\xi\Sigma_s$ is very similar to the map of minimum water abundance developed by Feldman et al. [1]. The mean fraction energy loss and scattering cross section are strongly dependent on hydrogen abundance and are relatively insensitive to other elements. The map of Σ_a is correlated with the map of $\xi\Sigma_s$, which may be partially explained by the fact that thermal neutron capture by hydrogen is non-negligible. The microscopic absorption cross section is 0.33 barns. The correlation coefficient was found to be $R^2=0.67$.

Using the map of minimum water abundance reported by Feldman et al. [1], we determined the contribution of hydrogen to the macroscopic absorption cross section of Martian materials at mid-latitudes. We then subtracted the hydrogen macroscopic cross section from our map of Σ_a to determine a map of the

absorption cross section of all elements other than hydrogen. The resulting map, shown in Fig. 7, is similar to the map of the total absorption cross section shown in Fig. 6. The correlation between Σ_a and $\xi\Sigma_s$ remains following the subtraction of the contribution from hydrogen ($R^2=0.55$).

The correlation of the absorption cross section for elements other than H with $\xi\Sigma_s$, which is directly related to the abundance of water-equivalent hydrogen, may indicate past processing of surface materials by water. The highest values in the absorption cross section occur northward of the dichotomy boundary in Acidalia Planitia and Utopia Planitia. These are lowlands in which standing water may have existed on or near the surface, possibly resulting in the formation of Cl-salts.

Conclusions: In this study, we analyzed thermal and epithermal neutron data to determine whether the composition of elements other than hydrogen varied significantly in the Martian mid-latitudes. We mapped the macroscopic absorption and scattering cross sections in the mid latitudes assuming there was no variation of composition with depth. The absorption cross section for elements other than hydrogen was found to be generally correlated with minimum water abundance. This suggests that the absorption cross section is sensitive to aqueous alteration of surface materials. The highest values in the absorption cross section occur northward of the dichotomy boundary in Acidalia Planitia and Utopia Planitia. These are lowlands in which standing water may have existed on or near the surface, possibly resulting in the formation of Cl-salts.

Comparison of measured count rates from three regions in Tharsis with simulated count rates for different materials shows that Tharsis materials are more consistent with basalt than with the mean Pathfinder soil composition. Lower Cl in basaltic materials may result in elevated thermal neutron count rates in the volcanic shield region and Solis Planum.

Capture gamma rays from Cl and Fe are detected by the gamma ray spectrometer. Maps of these elements with sufficient spatial resolution will be developed once sufficient counting precision is achieved. The abundance of Cl and Fe and the stratigraphy of water-equivalent hydrogen will eventually be determined through simultaneous analysis of both the neutron and gamma ray data. The neutron transport parameters we have mapped can be used to estimate the thermal neutron number density in the surface [8], enabling gamma ray counting data to be converted accurately into estimates of elemental abundance.

References: [1] Feldman W.C., et al. (2003) this proceedings, #3218. [2] Boynton, W.V., et al. (2002) *Science* 297, 81-85. [3] Tokar, R.L., et al. (2002) *Geophys. Res., Lett.* 29, doi:10.1029/2002GL015691. [4] Wanke H., et al. (2001) *Space Science Reviews* 96, 317-330. [5] Prettyman T.H. et al. (2003) *LPSC* 34, #1950. [6] Laul J.C., et al. (1986) *Geochim. Cosmochim. Acta* 50, 909-926. [7] Feldman W.C. et al. (2000) *JGR* 105, 20,347-20,363. [8] Lawrence D.J. et al. (2002) *JGR* 107, 10.1029/2001JE001530.

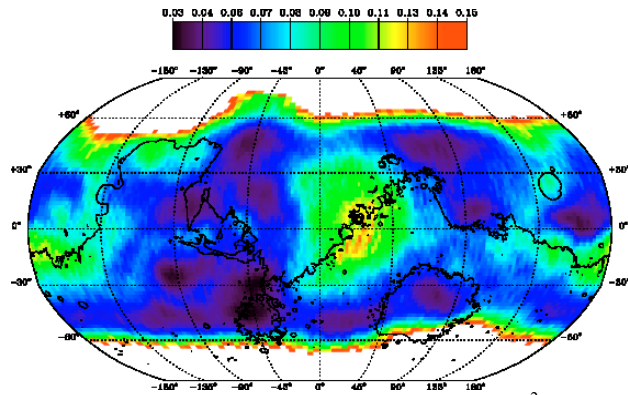


Fig. 4. Mid-latitude map of $\xi\Sigma_s$. The units are cm^2/g . A contour of topography at 0 km elevation is superimposed on the map.

Figure 7 (below). Mid-latitude map of the partial macroscopic absorption cross section (the contribution from hydrogen is removed). The units are $10^{-3} \text{ cm}^2/\text{g}$. A contour of topography at 0 km elevation is superimposed on the map.

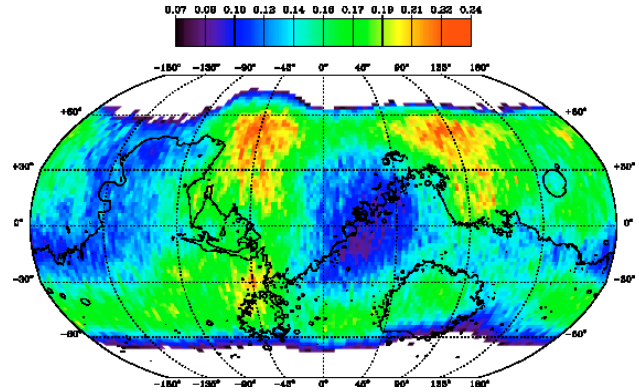
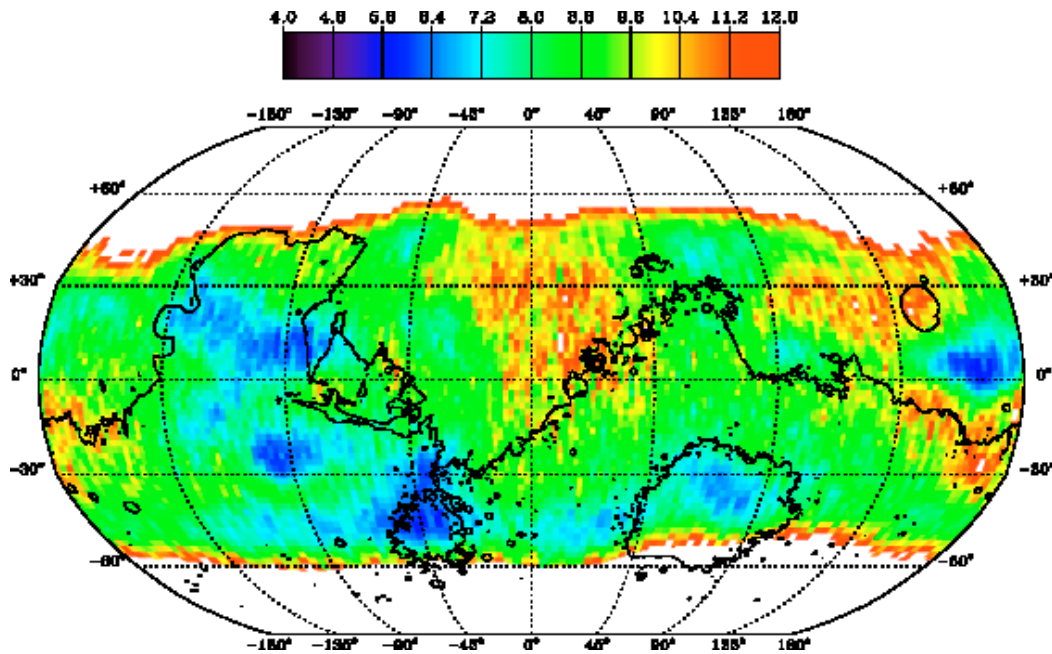


Fig. 5. Mid-latitude map of Δ . A contour of topography at 0 km elevation is superimposed on the map.

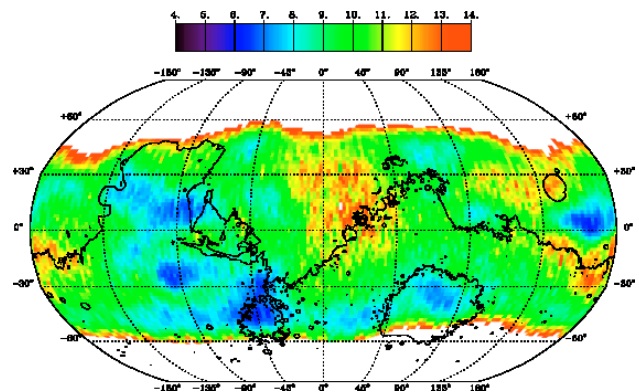


Fig. 6. Mid-latitude map of the total macroscopic absorption cross section, Σ_a . The units are $10^{-3} \text{ cm}^2/\text{g}$. A contour of topography at 0 km elevation is superimposed on the map.

THERMOPHYSICAL PROPERTIES OF THE MARTIAN SOUTH POLAR REGION. N. E. Putzig¹, M. T. Mellon¹, and R. E. Arvidson², ¹Laboratory for Atmospheric and Space Physics, University of Colorado, Boulder, CO 80309, ²McDonnell Center for the Space Sciences, Department of Earth and Planetary Sciences, Washington University, St. Louis, MO 63130. E-mail contact: putzig@colorado.edu.

Introduction: Previous analysis of thermal inertia and albedo data from the Mars Global Surveyor (MGS) Thermal Emission Spectrometer (TES) delineated three major surface thermophysical units [1, 2, 3]. A fourth unit of low thermal inertia and low-to-intermediate albedo was found to dominate the region poleward of 65°S [1]. We consider end-member geological explanations for this unit and conclude that reduced density in a relatively coarse-grained or indurated mantle is favored over theories invoking dark, unconsolidated dust. A mechanism for reducing bulk density by ablation of near-surface ground ice is suggested by results from the Mars Odyssey Neutron Spectrometer [4] and is supported by other theoretical [5] and TES spectral studies [6].

Background: Thermal inertia is the key surface property controlling diurnal temperature variations and is dependent on particle size, degree of induration, rock abundance, and exposure of bedrock within the top few centimeters of the subsurface (i.e., the thermal skin depth). It is a measure of the subsurface's ability to store heat during the day and to re-radiate it during the night. Thermal inertia is defined as the combination of bulk thermal conductivity k , bulk density ρ , and heat capacity C of the surface layer such that:

$$I \equiv \sqrt{k\rho C} . \quad (1)$$

For granular materials under Mars surface conditions, k dominates and is driven by the conductivity of gas in pore spaces, but it also depends on ρ [5]. Thus, a large change in bulk density may effect a significant change in thermal inertia.

In general, unconsolidated fines (i.e., dust) will have low values of thermal inertia, indurated dust (duricrust) and sand-sized particles will have intermediate values, and rocks and exposed bedrock will have high values. In the context of MGS observations, the thermal inertia of any given location on the Martian surface is generally controlled by a variable mixture of such materials on the scale of the TES observations (approximately 3 x 6 km). By considering thermal inertia together with other observed surface properties, one can gain insight into the physical characteristics of the surface and the geological processes which have affected it.

Methodology: We used global maps of thermal inertia and albedo from [2], MOLA elevation, MOC images, and Viking MDIM 2.0 and color data in our analysis. The thermal inertia map was derived from

nighttime (approximately 2 AM local time) thermal bolometer observations of surface temperature gathered during TES orbits 1583-11254, covering over one Mars year (L_s 103° to 360° + 0° to 152°) [2,3]. The mapping process employed filters to eliminate observations from periods of high water-ice-cloud and atmospheric-dust opacity and completely excludes orbits 4199-5410, due to the 1999 global dust storms. Map overlays and two-dimensional histograms between the various datasets were used to delineate areas with common features and to assign mapping units.

Thermophysical Unit Definition: Previous analyses [2, 3] of MGS-TES derived thermal inertia identified three regions of distinct albedo and thermal inertia. These have been interpreted as surfaces dominated by (A) unconsolidated fines; (B) courser-grained sediments, rocks, bedrock exposures, and some duricrust; and (C) duricrust with some rocks and/or bedrock exposures. In Figure 1, we show unit boundaries revised from those defined in [1], wherein the thermal inertia-albedo parameter space was further subdivided into regions of (D) low thermal inertia and low-to-intermediate albedo; (E) very low albedo; (F) very low thermal inertia and high albedo; and (G) very high thermal inertia and high albedo.

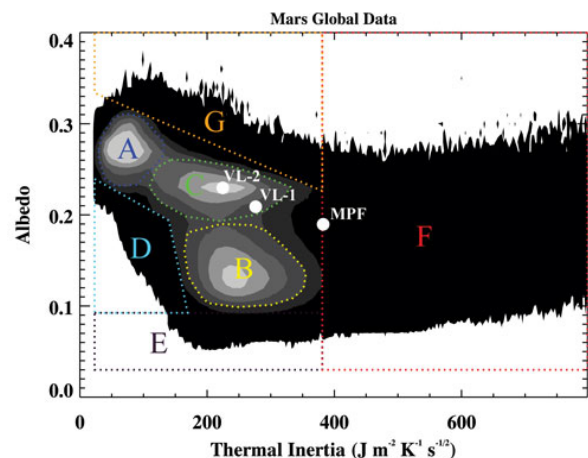


Figure 1: Global correlation between thermal inertia and albedo. Unit letters correspond to those in Figure 2.

very high thermal inertia; and (G) very high albedo. Figure 2 provides an orthographic map of these units centered on the South Pole, showing their areal distribution in the southern hemisphere. Unit D (light blue) exhibits distinct low-thermal-inertia boundaries (compare Figure 3), making it unique from surrounding

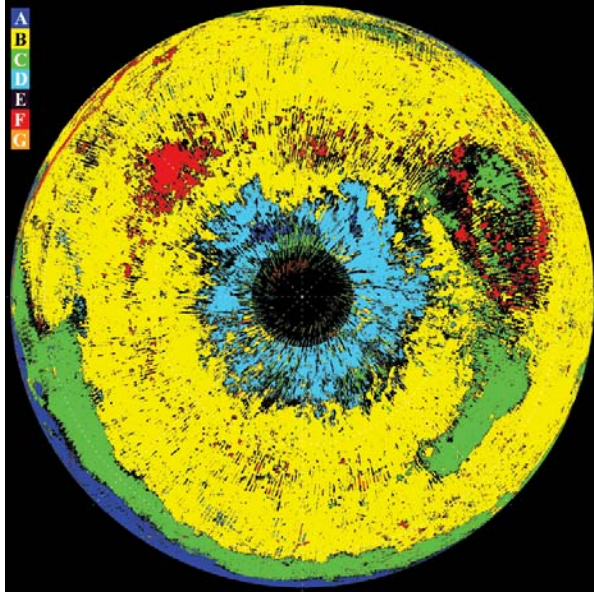


Figure 2: Thermal inertia-albedo unit map of the southern hemisphere of Mars (filled from equator to 80°S). Unit letters correspond to those in Figure 1.

higher thermal inertia Units B (yellow) and C (green). Unit D dominates the region south of about 65°S.

End-member Hypotheses: The low thermal inertia values of Unit D, which are similar to those of Unit A, are normally considered to be indicative of fine-grained, unconsolidated materials. However, the albedo of Unit D, which is comparable to that of Unit B, is much lower than that of Unit A. These observations lead to two end-member scenarios. The first involves a reduction in thermal inertia in a material that is otherwise similar to that in Unit B, which can be achieved by lowering bulk conductivity. The second involves a reduction of albedo in a material that is otherwise similar to that in Unit A, either through a compositional difference or a darker coating on individual grains.

Thermal Inertia Reduction: Unit D may represent a surface of either indurated fines or coarser grained materials in which the bulk thermal conductivity has been lowered. Laboratory data (Figure 4) show a linear dependence of thermal conductivity on density with a slope of about $0.0225 \text{ W m}^2 \text{ kg}^{-1} \text{ K}^{-1}$ [5]. Using Equation (1) and assuming a constant heat capacity, we calculate that the observed 2-fold reduction in thermal inertia from Unit B to Unit D would require about a 2.5-fold reduction in density. Recent estimates of ground ice in the top meter of the Martian surface based on data from the Mars Odyssey Neutron Spectrometer [4] predict ice content up to 75% by volume in the polar regions. In the upper few centimeters (the TES sensing depth), ice is seasonally unstable and is

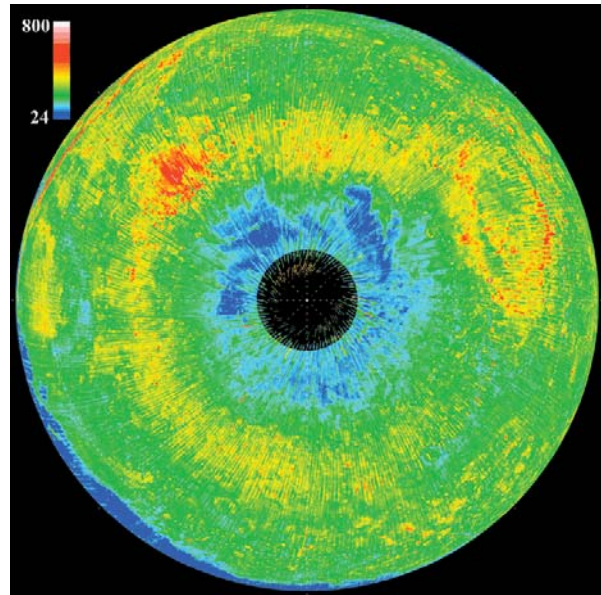


Figure 3: Thermal inertia map of the southern hemisphere of Mars (filled from equator to 80S). After Mellon *et al* (2002). Compare polar low thermal inertia region to Unit D in Figure 2.

expected to ablate. It is conceivable that such an ablation zone may produce a near surface with greatly expanded pore volume and reduced bulk density.

A regional analysis of thermal inertia-albedo correlation provides additional support for this thermal inertia reduction scenario. We generated a series of a 2D histogram of thermal inertia and albedo restricted to various southern latitudes, and found a single broad peak spanning the region between Units B and D (see Figure 5). This peak migrates from Unit B to Unit D with increasing southerly restriction of latitudes. Additionally, we examined MOC images from each Unit as well as some which extend across the Unit boundary and found a mantled appearance in both regions. Images over Unit D showed more polygonal and cracked surfaces, whereas those over Unit B were generally smoother. However, we have found no abrupt morphological changes over the Unit boundaries. Taken together, these results suggest that the two units may be compositionally related.

Albedo Reduction: Alternatively, Unit D may represent a surface of fine-grained, unconsolidated materials of a composition which is either distinct from that in Unit A (implying a distinct source material for dust), or the same as that in Unit A but altered by a darkening process. In the first case, the darker material might be either a layer which is thermally thin (but optically thick; \sim few μm) overlying a bright dust similar to that in Unit A, or a thicker dark layer with similar thermal properties to that in Unit A. In the second

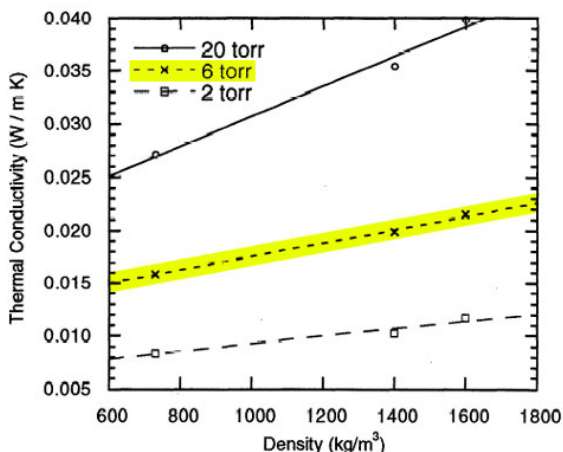


Figure 4: Thermal conductivity versus bulk density for 25-30 μm particles at three atmospheric pressures. That corresponding to Mars surface conditions is highlighted. From Presley and Christensen [5].

case, the individual grains of an initially bright dust may be coated by a darker material (presumably by some chemical process which is restricted to the south polar zone).

A major problem with these dark dust theories is the fact that global dust storms on Mars are expected to homogenize unconsolidated fines over years to decades [7]. It is therefore difficult to maintain a large region covered with a darker dust over extended periods. However, Viking results [8] show a similar pattern of low thermal inertia in this region, so it is unlikely that this is a transient phenomenon. Also, a dust cover index map [6] produced from TES spectra indicates that there is little or no unconsolidated dust in the region shown as Unit D in Figure 2.

Summary: We have identified an unusual region of low thermal inertia and low albedo which dominates the south polar region of Mars. While its thermal inertia is consistent with lower resolution data from Viking [8], this region differs from the classic low thermal inertia regions at mid-latitudes in that the latter are characterized by high albedo. We considered hypotheses to explain this observation, involving either a reduction of thermal inertia in Unit B material or a reduction of albedo in Unit A material. Several independent lines of evidence support a reduction in thermal inertia obtained by a reduction in bulk density, whereas albedo reduction theories encounter problems with the homogenization of fines expected to occur due to global dust storms.

The density reduction theory favored here fails to explain the lack of a similar phenomenon in the north polar region. The latest Odyssey neutron data [9]

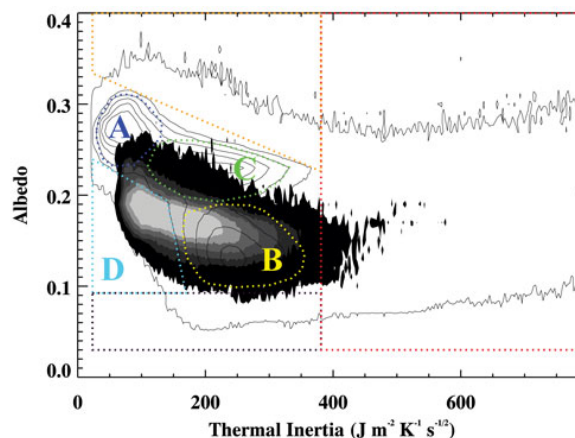


Figure 5: Correlation between thermal inertia and albedo for the globe (unfilled contours) and 60°S to 80°S (filled contours). Unit letters as in Figures 1 and 2.

show even more extensive ground ice in the north than in the south, so one might expect a similar process to occur there. While the current thermal inertia map actually shows a zone of high thermal inertia at most longitudes northward of 70°N, this is not in keeping with Viking results [10], and these high values are believed to be caused by a model or observational artifact and not reflective of the actual surface [2]. Nevertheless, we see no indication of a regional reduction of thermal inertia in the north in those regions where the data appear to be more reliable. Further effort to correct this problem and to fully characterize the north polar region may help resolve this issue.

The concepts discussed here represent end-members and it is possible that the true cause of this phenomenon may have multiple sources. Furthermore, intermediate explanations are not currently distinguishable. For example, smaller reductions in both albedo and thermal inertia in Unit C material might serve to produce all or part of the results observed in Unit D.

References: [1] Putzig *et al* (2003) *LPSC XXXIV*. [2] Mellon *et al* (2002) *LPSC XXXIII*. [3] Mellon *et al* (2000) *Icarus* 148. [4] Boynton *et al* (2002) *Science* 297. [5] Presley & Christensen (1997) *JGR* 102 E4. [6] Ruff & Christensen (2002) *JGR* 107 E12. [7] Kahn *et al* (1992) in *Mars*, Kieffer *et al*, eds., U. of Az. [8] Paige & Keegan (1994) *JGR* 99 E12. [9] Boynton (2003) *Verdanasky-Brown Microsymposium* 37. [10] Paige *et al* (1994) *JGR* 99 E12.